Continental rift architecture and patterns of magma migration: A dynamic analysis based on centrifuge models

Giacomo Corti,[1] Marco Bonini,[2] Dimitrios Sokoutis,[3] Fabrizio Innocenti,[1]
Piero Manetti,[4] Sierd Cloetingh,[3] and Genene Mulugeta[5]

Received 9 July 2003; revised 17 November 2003; accepted 26 November 2003; published 2 April 2004.

[1] Small-scale centrifuge models were used to investigate the role of continental rift structure in controlling patterns of magma migration and emplacement. Experiments considered the reactivation of weakness zones in the lower crust and the presence of magma at Moho depths. Results suggest that surface deformation, which reflects the weakness zone geometry, exerts a major control on patterns of magma migration. In the case of a single rift segment, the experimental lower crust and magma were both transferred in an extension-parallel direction toward the rift flanks. This lateral migration reflected the dominance of far-field stresses over extension-induced buoyancy forces. Local pressure gradients favored the raise of experimental magma in correspondence of marginal grabens. The lateral migration gave rise to major accumulations below the footwall of major boundary faults, providing the magma source able to feed off-axis volcanoes in nature, as inferred for the Main Ethiopian Rift. In the case of two offset rift segments, a major transfer zone developed. This transfer zone was characterized by prominent experimental lower crust doming and strong magma accumulation. Dynamic analysis showed that the transfer zone development caused a strong pressure difference in a rift-parallel direction, which dominated over the far-field thinning. Owing to this pressure gradient, almost all the underplated experimental magma collected below the lower crust dome, suggesting a rift-parallel (extension-orthogonal) migration. This process has a direct relevance for the localization of magmatic activity at transfer zones in natural continental rifts, such as in the Western Branch of the East African Rift System. *INDEX TERMS:* 8020 Structural Geology: Mechanics; 8109 Tectonophysics: Continental tectonics—extensional (0905); 8159 Tectonophysics: Rheology—crust and lithosphere; 8434 Volcanology: Magma migration; *KEYWORDS:* continental rifting, magma migration, analogue modeling. **Citation:** Corti, G., M. Bonini, D. Sokoutis, F. Innocenti, P. Manetti, S. Cloetingh, and G. Mulugeta (2004), Continental rift architecture and patterns of magma migration: A dynamic analysis based on centrifuge models, *Tectonics*, *23*, TC2012, doi:10.1029/2003TC001561.

1. Introduction

[2] The development of continental rifts is accompanied by the emplacement of significant volumes of magma at various crustal levels. Decompression of the lower lithosphere and upper asthenosphere, related to the mechanical stretching of the lithosphere, cause their partial melting and the diapiric rise of melts into the zone of lithospheric thinning [*Ziegler and Cloetingh*, 2003]. The volumes and the petrological-geochemical characteristics of the magmatic products are related to the thermal state of the asthenosphere and lithosphere at the onset of extension, the amount of lithospheric extension, the strain rates, the thickness of the lithosphere, the presence of volatiles and the relative motion of the diverging plates [e.g., *Ziegler and Cloetingh*, 2003, and references therein]. Conversely, the spatial distribution of the magmatic activity may be strongly influenced by rift kinematics and the resulting structural patterns [*Corti et al.*, 2003]. Previous experimental work has shown that rift-parallel intrusions may form on the shoulders of rift valleys during orthogonal extension [*Bonini et al.*, 2001], whereas en echelon oblique-trending magmatic bodies can be expected within the main rift depression during oblique rifting [*Corti et al.*, 2001]. Models of transfer zones have shown that a feedback interaction between magma emplacement and strain localization may develop during this process, facilitating the accumulation of large volumes of magma in transfer zones [*Corti et al.*, 2002, 2003].

[3] In this paper we use the results of centrifuge models, partly published by *Corti et al.* [2003], to discuss quantitatively the mechanisms activating magma migration during continental rifting and their relations with the deformation process. These experiments addressed the problem in a specific way by taking into account the reactivation of inherited zones of weakness in the lower experimental crust in order to reproduce different architectures of continental rift sys-

[1]Dipartimento di Scienze della Terra, Università degli Studi di Pisa, Pisa, Italy.
[2]CNR–Istituto di Geoscienze e Georisorse, Sezione di Firenze, Florence, Italy.
[3]Netherlands Center for Integrated Solid Earth Science, Faculty of Earth and Life Sciences, Vrije Universiteit Amsterdam, Amsterdam, Netherlands.
[4]CNR–Istituto di Geoscienze e Georisorse, Pisa, Italy.
[5]Hans Ramberg Tectonic Laboratory, Institute of Earth Sciences, Uppsala University, Uppsala, Sweden.

0278-7407/04/2003TC001561$12.00

tems. We present a detailed dynamical analysis of model deformation that shows how migration of magma during rifting is primarily controlled by lateral pressure variations and the related buoyancy forces resulting from heterogeneous stretching of the brittle upper continental crust. This analysis provides two major models for the migration of magma during rifting that have an important relevance for understanding the dynamics of major processes in nature such as the off-axis volcanism (as in the Main Ethiopian Rift) and the localization of magmatic activity at transfer zones (as in the Western Branch of the Main Ethiopian Rift).

2. Analogue Modeling

[4] The experimental concept behind the current series of models is based on the assumption that the thermomechanical process of continental rifting results from the application of extensional stresses to a pre-deformed, and thus already structured, anisotropic lithosphere. As a consequence, rift structures are not randomly distributed but tend to follow the trend of ancient orogenic belts, avoiding stronger cratonic regions [e.g., *Dunbar and Sawyer*, 1989; *Versfelt and Rosendahl*, 1989]. It has been shown that rift segments propagate along inherited anisotropies and tend to link together in correspondence to transverse pre-existing fabrics, giving rise to transfer zones [*Versfelt and Rosendahl*, 1989]. In nature, rheological heterogeneities, which lead to strain localization and control both rift location and its structural pattern, tend to occur throughout the whole lithosphere [e.g., *Tommasi and Vauchez*, 2001; *Ziegler and Cloetingh*, 2003]. Pre-existing faults and shear zones represent a mechanical weakness at upper and lower crust levels [e.g., *Daly et al.*, 1989], and within the pre-deformed regions the total strength of the lithosphere is expected to decrease as a result of an increase in lateral rheological heterogeneity within the lower crust [e.g., *Dewey*, 1986; *Dunbar and Sawyer*, 1989]. On the basis of these arguments, we introduced a weakness zone in the lower crust (WLC) to localize strain in the overlying brittle upper crust [*Corti et al.*, 2003]. By varying the geometry of this weakness zone we reproduced different architectures of interacting rift segments and different patterns of the transfer zones. Petrologic studies on the magmatic products outcropping in continental rifts have documented that magmatism is contemporaneous with, or begins shortly before, extension [e.g., *Baker et al.*, 1972; *Ramberg and Morgan*, 1984; *Morgan et al.*, 1986; *Ebinger*, 1989a, 1989b; *Ruppel*, 1995; *Faulds and Varga*, 1998], suggesting that magmatic bodies are present within the system from at least the first stages of extension and may play an important role in the evolution of deformation. Following these observations, we have simplified the evolution of the rift system by assuming initial conditions characterized by the presence of an underplated, partially molten body that is less dense than the overlying crust and ductile upper lithospheric mantle. The initial magma-ponding zones were pre-determined by assuming that underplating is roughly parallel to the trend of the weakness zones. This initial configuration is a reasonable simplification of the natural rifting, where initial underplating is controlled by thermal anomalies resulting from the ponding of deep hot materials [e.g., *Hill*, 1991; *Ebinger and Sleep*, 1998].

2.1. Experimental Setup

[5] Experiments were performed at 200 g in an artificial gravity field, using the Large Capacity Centrifuge at the Hans Ramberg Tectonic Laboratory of Uppsala University, Sweden [*Ramberg*, 1981] Following the work of *Bonini et al.* [2001], the rheologically layered models were built in a Plexiglas box and bounded by rectangular blocks of plasticine that were gradually removed during successive runs in the centrifuge (Figure 1) [*Corti et al.*, 2003]. The models thus underwent a vertical thinning and lateral expansion in response to the centrifugal body force field simulating gravity in nature.

[6] The experimental set-up simulated a weakness zone in the lower crust (WLC) whose geometry was varied in various experiments to reproduce two interacting offset rift segments and to study the architecture of the deformation pattern in the overlying brittle crust (Figure 1). In nature, adjacent rift segments are typically offset from each other in the strike direction, so that rift systems typically exhibit major kinks [e.g., *Versfelt and Rosendahl*, 1989] (Figure 1b). To reproduce such geometries, we varied the angle (ϕ) between the WLC segment in the transfer zone and the rift trend by changing the overlap (L) between the two offset rift segments (i.e., the on-axis distance between the adjacent rift segments) and keeping the overstep (S) constant [e.g., *Acocella et al.*, 1999a; M. A. Naylor and J. A. M. van Gool, unpublished work in *Mechanics of Tectonic Faulting* edited by G. Mandl, Elsevier Sci., New York, 1988] (Figure 1 and Table 1).

2.2. Materials

[7] In the experiments, quartz-sand was used to simulate the brittle upper crust, whereas various viscous materials represented the ductile lower crust and upper mantle [*Corti et al.*, 2003]. The weak lower crust (WLC) was simulated by a low exponent power law sand-silicone mixture with a density of 1520 kg/m^3; plasticine was added to this mixture to increase its resistance without altering density (1540 Kg/m^3) and hence to simulate the ''normal'' lower crust (LC). The uppermost part of the lithospheric mantle was reproduced using a low-exponent power law sand-silicone mixture with a density of 1580 kg/m^3. Glycerol was used to simulate magma. Table 2 summarizes the details about the material parameters. Model strength profiles, illustrated in Figure 2d, show that the experimental lithosphere is characterized by two strength peaks, one at the base of the brittle upper crust and the other one in the uppermost lithospheric mantle. This latter layer has a resistance which is slightly lower than the model upper crust, well approximating natural conditions characterized by high geothermal gradients resulting in high Moho temperatures [e.g., *Ranalli*, 1995,

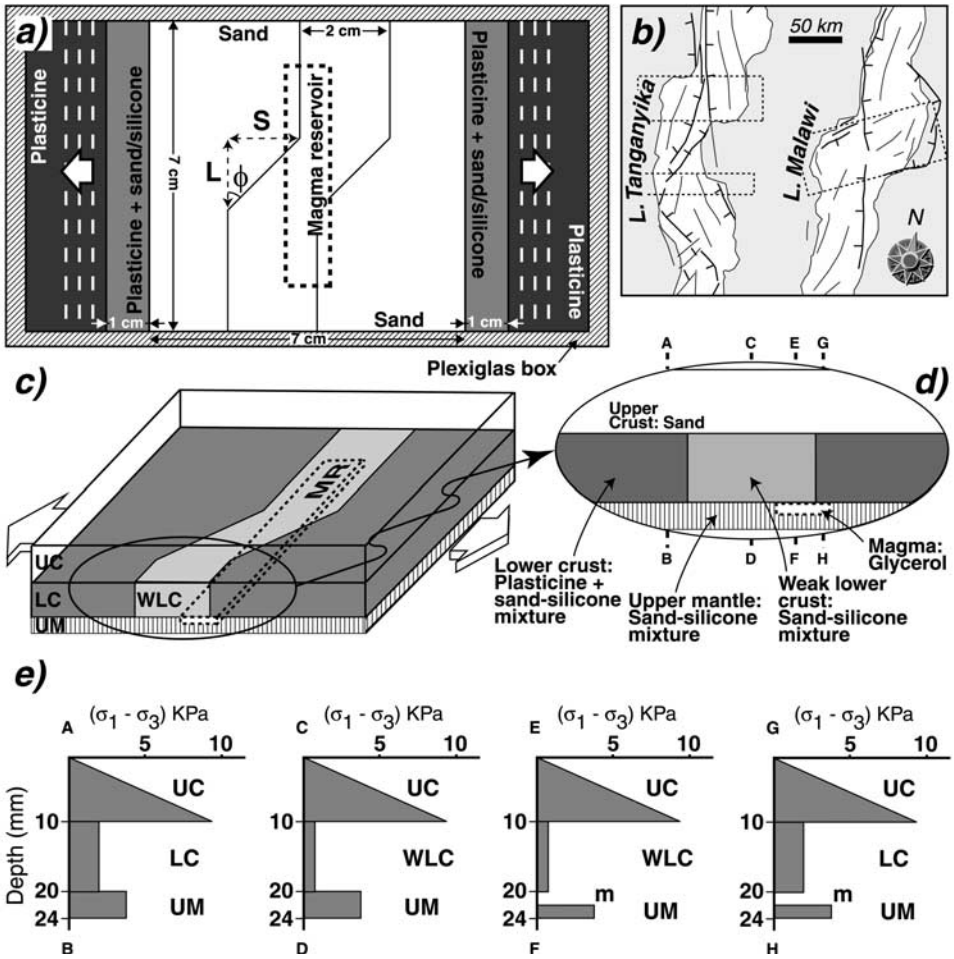

Figure 1. (a) Model top view showing the experimental setup of the NRTZ series of models. (b) Schematic fault pattern in Lakes Malawi and Tanganyika [*Versfelt and Rosendahl*, 1989] (used with permission from *Nature* (http://www.nature.com)) showing the typical staircase rift segments offset (dashed rectangles). (c) Schematic 3-D view and (d) cross section illustrating the experimental rheological stratification. (e) Initial strength profiles calculated in different regions of the model, indicated in Figure 1d by the letters A–B, C–D, E–F, G–H. For details about the calculations of strength profiles and the resistance of experimental layers see Appendix A. In Figure 4, L and S are the overlap and overstep between the two offset segments of the weak lower crust, respectively [e.g., *Acocella et al.*, 1999a]. During our experiments, S was kept constant (S = 1.5 cm), whereas L was varied in order to explore angles ϕ of 0°, 25°, 45° and 90°. UC: upper crust; LC: lower crust; WLC: weak lower crust; UM: upper mantle; MR: initial magma reservoir; m: experimental magma.

and reference therein]. Details about calculations of the strength profiles, the resistance of single layers and the total strength of the experimental lithosphere are reported in Appendix A.

2.3. Model Scaling

[8] Scaling of the models follows the principles of dynamic similitude [e.g., *Ramberg*, 1981]. The models were intended to represent a length scale of $h^* \approx 5.5 \times 10^{-7}$ (where h^* is the ratio of length in the model, l_m, to the corresponding length in nature, l_n), such that 1 cm in the model corresponds to ≈18 km in nature and the model crust represents a ≈35-km thick continental crust with a ≈4-km thick zone of magmatic underplating.

[9] For testing dynamic similitude between models and nature we calculated dimensionless ratios of stresses acting in the system [*Ramberg*, 1981] (see section A4 in Appendix A and Table 3). For viscous deformation, we calculated the ratio of gravitational to viscous stresses, *Rm*, Ramberg number [*Weijermars and Schmeling*, 1986]. Analogously, we calculated the ratio of gravitational to cohesive stresses for the brittle deformation, *Rs* [see *Ramberg*, 1981; *Mulugeta*, 1988]. Since both models and nature share similar *Rm* and *Rs* numbers, we assume that

Table 1. Parameters of Model Deformation for Experiments of the NRTZ Series

Model	Angle Between the Weak Lower Crust Segments (ϕ), deg	Average Velocity of Extension, mm/s	BC:DC	Magma Chamber Geometry	Amount of Extension, β
NRTZ1	45°	$2.1\ 10^{-1}$	1:1	no magma	1.50
NRTZ5	90°	$2.7\ 10^{-1}$	1:1	orthogonal (5 × 1 cm)	1.45
NRTZ6	45°	$2.5\ 10^{-1}$	1:1	orthogonal (5 × 1 cm)	1.51
NRTZ7	25°	$2.4\ 10^{-1}$	1:1	orthogonal (5 × 1 cm)	1.53
NRTZ8	0°	$2.1\ 10^{-1}$	1:1	orthogonal (5 × 1 cm)	1.50

the experiments are dynamically scaled and simulate a reasonable ≈6 mm yr^{-1} natural extension rate [e.g., *Chu and Gordon*, 1999] (section A4 in Appendix A and Table 3). The scaling to nature of the total resistance of the lithosphere and the forces driving extension of models is discussed in section A5 of Appendix A.

3. Experimental Results

3.1. Surface Fault Pattern

[10] The pattern of model surface deformation shown in Figure 2 illustrates how the WLC localizes deformation in the overlying brittle crust, so that the geometry of the WLC and the angle ϕ (offset angle between WLC segments) are able to exert a strong influence on the architecture of the rift system [*Corti et al.*, 2003].

[11] When $\phi = 0°$ (i.e., a straight WLC is present in the center of the model; model NRTZ8; Figure 2a), the deformation is accommodated by normal faulting above the WLC-LC rheological boundaries. Particularly, this fault pattern gives rise to two narrow grabens, trending orthogonally to the extension direction. A detailed analysis of the model cross sections reveals that these grabens bound a major topographically depressed area, corresponding at depth to a marked thinning of the weak ductile crust in the central part of the model. The two lateral grabens can be interpreted as marginal grabens delimiting a main rift zone (Figure 3a), a structural pattern documented in previous analogue models [*Mulugeta and Ghebreab*, 2001] and characteristic of natural continental rifts [*Scholz and Contreras*, 1998].

[12] For $\phi = 25°$ (model NRTZ7; Figure 2b), two narrow oblique-trending grabens are recognizable at the model surface and closely follow the trend of the WLC-LC rheological interfaces. As in model NRTZ8, these grabens border a major topographic depression that developed in the central part of the model. Within this major depression,

Table 2. Characteristics of Experimental Materials for the Different Series

Material	Prototype Layer	Thickness, mm	Density, kg m^{-3}	Coefficient of Internal Friction	Cohesion	Rheological Characteristics	Power Law Parameters[c]
Sand[a]	upper crust	10	1360	$\mu = 0.6$	400 Pa s[b]	brittle behavior	
Sand + Rhodorsil Gomme 70009 (manufactured by Rhone Poulenc, France)	weak lower crust	10	1520			power law	n = 1.2 A = $1\ 10^{-5}$
Plasticine + sand + Rhodorsil Gomme 70009 (manufactured by Rhone Poulenc, France)	lower crust	10	1540			power law	n = 1.6 A = $1.5\ 10^{-7}$
Sand + Rhodorsil Gomme 70009 (manufactured by Rhone Poulenc, France)	upper mantle	4	1580			power law	n = 1.2 A = $1.5\ 10^{-6}$
Glycerol	magma	2	1260			Newtonian behavior	≈1 Pa s[d]

[a]The sand was soaked with paraffin oil to enhance cohesion and to avoid its collapse when inserting the models vertically in the centrifuge.
[b]After *Bonini et al.* [2001].
[c]Measured at room temperature (≈23°C).
[d]After *Cruden et al.* [1995].

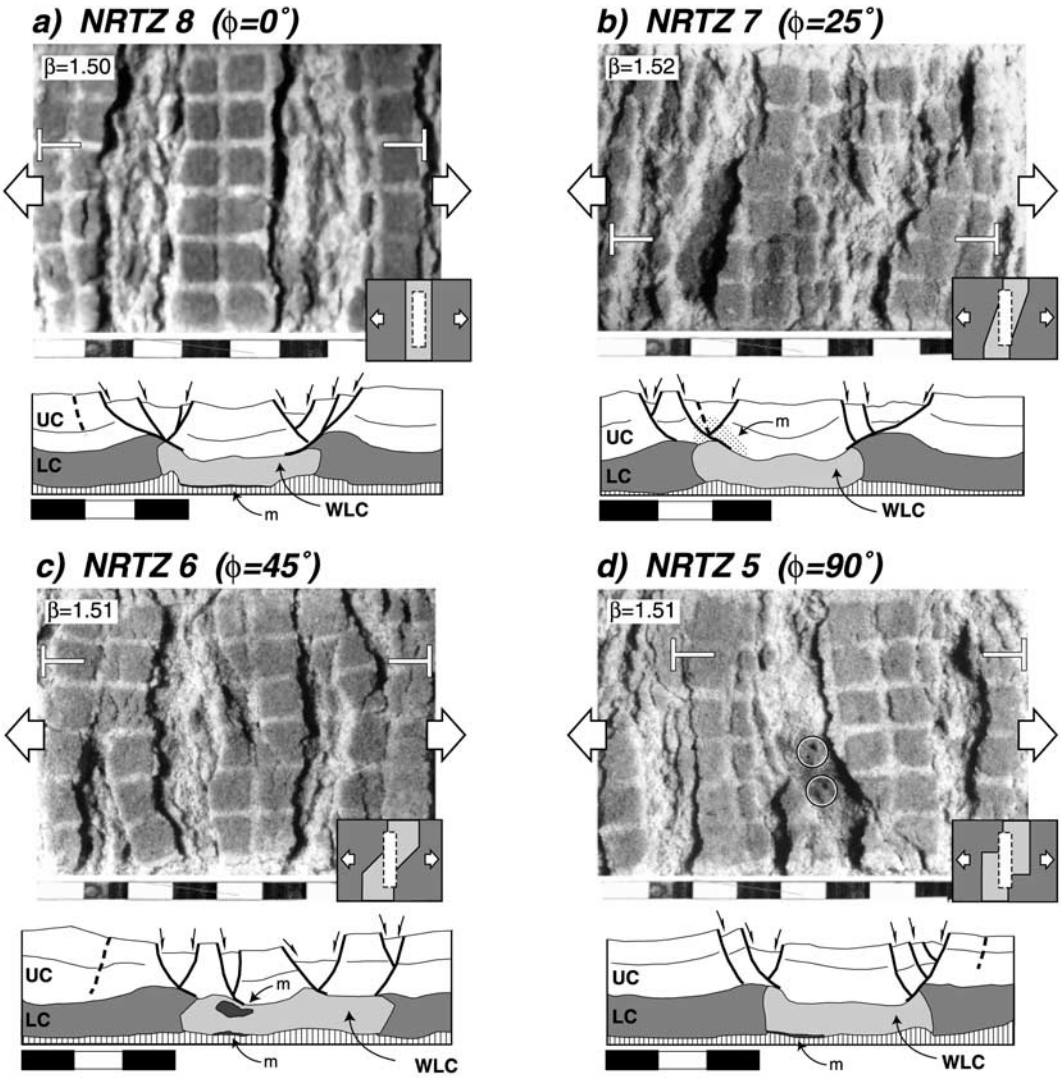

Figure 2. Top view and cross section of models with subcrustal magmatic underplating. The insets show the initial geometry of the rheological discontinuity (WLC) as well as the initial position of the experimental magma reservoir. The trace of the cross section is indicated in white on the top surface of the model. The two small circles in Figure 2d are spots of magma outcropping at the surface. Scales are in centimeters.

extension in the brittle layer was accommodated by oblique fault segments, with a strike opposite to that of the WLC step, that nucleated from the early stages of deformation (Figure 2b).

[13] High ϕ values (>45°) result in more complex surface fault patterns. For ϕ = 45° (model NRTZ6; Figure 2c), the surface fault pattern consisted of a larger number of fault sets, with a fault throw and graben width that is less

Table 3. Scaling Parameters for Brittle and Ductile Deformation at the Onset of Extension[a]

ρ_d Lower Crust Density, kgm^{-3}	ρ_b Upper Crust Density, kgm^{-3}	g Gravitational Acceleration, m s^{-2}	h_d Lower Crust Thickness, m	h_b Upper Crust Thickness, m	μ Coefficient of Internal Friction	λ Hubbert-Rubey Coefficient	τ_c Cohesive Strength, Pa	V Extension Rate, m s^{-1}	$\dot{\varepsilon}_x$ Strain Rate, s^{-1}	R_m[b]	R_s
Models 1540	1360	1962	$1\ 10^{-2}$	$1\ 10^{-2}$	0.6	0.5	400	$2.5\ 10^{-4}$	$1.2\ 10^{-2}$	17	2.8
Nature 2950	2700	9.81	$1.8\ 10^{4}$	$1.8\ 10^{4}$	0.6	0.42	$60\ 10^{6}$	$1.9\ 10^{-10}$	$5\ 10^{-15}$	10	2.0

[a]See section A4 in Appendix A for details of calculations.
[b]Calculated for the lower crust.

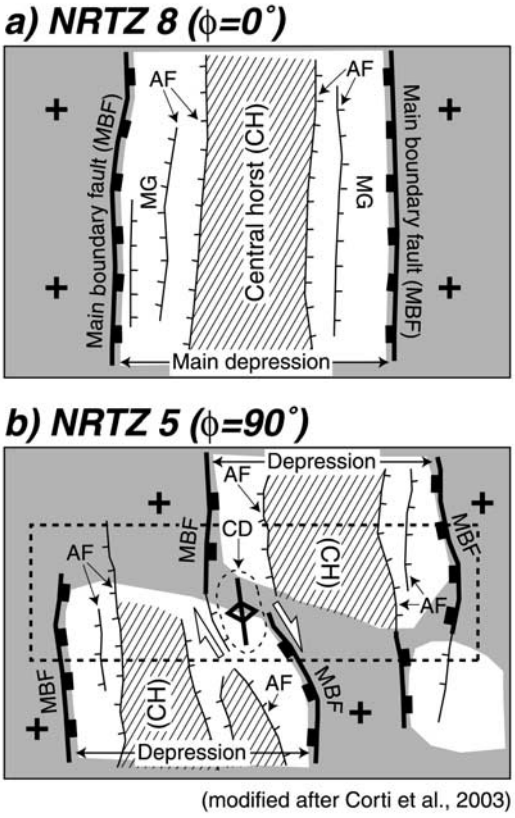

Figure 3. Line drawing of the surface deformation of models NRTZ8 (a) and NRTZ5 (b). Deformation in model NRTZ8 ($\phi = 0°$) consists of a single main depression, and in model NRTZ5 ($\phi = 90°$) consists of two offset depressions. The central dome in Figure 3b corresponds to the experimental magma spots shown in Figure 2d. The plus symbol indicates the uplifted regions corresponding to the rift flanks, while the depressed areas are in white. The dashed rectangular box marks the position of the transfer zone. AF: antithetic faults; CH: central horst; MBF: main boundary faults; CD: central dome. Figure 3b is modified after *Corti et al.* [2003] (with permission from Elsevier Science).

pronounced than in models NRTZ7 (Figure 2b) and NRTZ8 (Figure 2a). This can be seen by comparing the final top views of the models (cf. Figure 2c with Figures 2a and 2b). At least three distinct fault sets can be distinguished on the surface of model NRTZ6. One set consists of short fault segments developing at the bottom left and top right corners, which nucleated from the WLC-LC rheological boundaries and propagated perpendicularly to the extension direction above the LC (Figure 2c). The major fault set consists of two parallel narrow bands of deformation that are clearly influenced by both the WLC-LC boundaries and the initial glycerol reservoir. These faults nucleated at WLC-LC interfaces and propagated along-strike, following the perturbation induced by the presence of the low-viscosity glycerol. The third set is composed of faults bordering a small oblique graben that developed in the axial part of model NRTZ6, with a trend that was again opposite to that of the WLC step (Figure 2c).

[14] When $\phi = 90°$ (model NRTZ5; Figure 2d), the surface fault pattern is characterized by three distinct grabens. As in model NRTZ6, the two external grabens were bordered by normal faults that nucleated at the WLC-LC boundaries and propagated along-strike. These faults and the corresponding grabens are perpendicular to the extension direction. The most pronounced graben developed in the central part of the model; its greater width documents that this structure accommodated much of the deformation (Figure 2d). This graben was oblique to the extension direction corresponding to the right angle offset between the two WLC segments; as a consequence, the boundary normal faults developed a component of dextral shearing (Figure 2d). Analysis of surface topography suggests that the overall structural pattern can be interpreted in terms of two major offset depressions delimited by marginal grabens and linked by a transfer zone containing overlapping border faults with alternating polarity (Figure 3b).

3.2. Influence of Glycerol (Experimental Magma) on Surface Fault Patterns

[15] The current experiments have demonstrated that the presence of glycerol (the experimental magma) in the model setup has a strong influence on surface fault patterns. This is clearly illustrated by comparing the final structural pattern of model NRTZ6, with an initial sub-crustal glycerol reservoir, and model NRTZ1, with no glycerol (Figure 4).

[16] In model NRTZ1, deformation is accommodated by two conjugate normal fault systems orthogonal to the direction of extension, which delimit a central depression (Figure 4). At the WLC offset, these faults curve following the geometry of the WLC-LC rheological boundaries and give rise to a transfer zone. This transfer zone consists of a major fault set with a trend opposite to the WLC offset and with an angle of $\approx 45°$ to the extension direction. These oblique faults, mainly characterized by oblique-slip kinematics, cut across the rift depression and link the two border fault systems (Figure 4a).

[17] In model NRTZ6, the extension-orthogonal fault systems are more complex, as they preferentially followed the geometry of the initial glycerol reservoir rather than that of the WLC-LC rheological boundaries, reflecting the perturbation induced by the lateral flow of the experimental magma (Figure 4b). As a consequence of strain localization above the low-viscosity body, the oblique faults developing within the transfer zone were not able to connect the two oppositely dipping normal fault systems and their angle with the direction of extension is higher ($\approx 70°$) than in model NRTZ1 (Figure 4b). This behavior highlights again the mechanical influence on deformation exerted by the presence of the low-viscosity glycerol body.

3.3. Ductile Doming and Experimental Magma Emplacement

[18] Three-dimensional internal deformation analysis of the models shows two end-member patterns of ductile

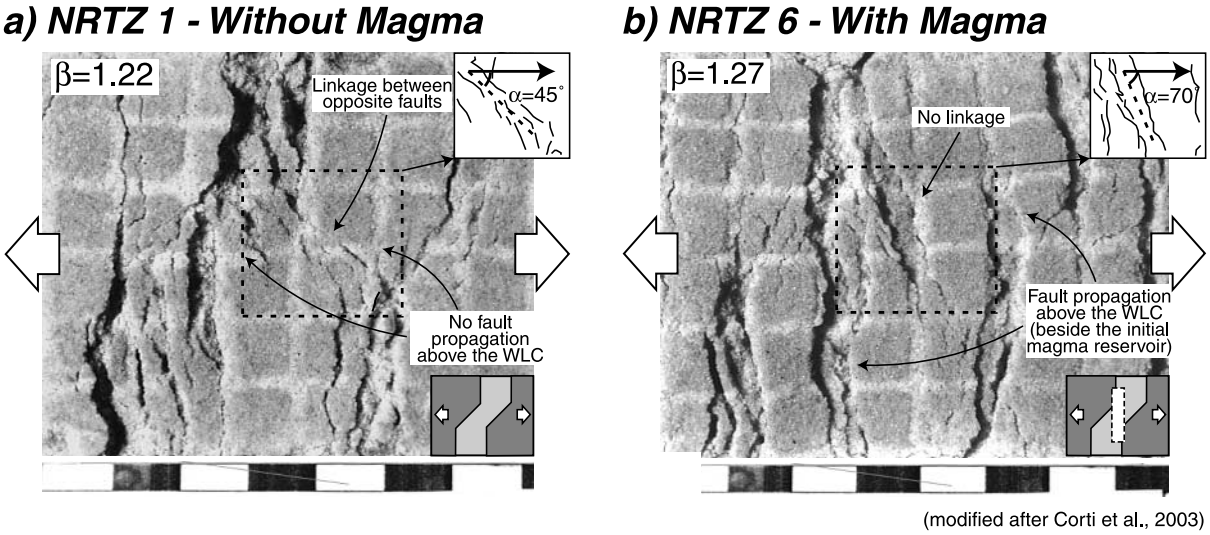

Figure 4. Comparison between models performed (a) without underplating and (b) with an initial sub-crustal experimental magma reservoir (both models have $\phi = 45°$). Insets show the initial model setup, as well as the angle between the trend of oblique faults within the transfer zone and the extension direction. Scales are in centimeters. Modified after *Corti et al.* [2003] (with permission from Elsevier Science).

doming and experimental magma emplacement (Figure 5) [*Corti et al.*, 2003]. These patterns of doming, observed in the two distinct cases of $\phi = 0°$ (single narrow rift) and $\phi = 90°$ (offset rift segments), also correspond to different flow directions of glycerol within the models.

[19] In the case of a single main depression ($\phi = 0°$, model NRTZ8), the experimental magma was transferred laterally from its central position toward the cores of lower crustal domes forming at the WLC-LC boundaries. We refer to them as "external domes" (ED; Figure 5a). The model cross sections reveal that these external domes correspond to a relative thickening of the model lower crust below the marginal grabens, as elucidated by the analysis of the thinning factor $1/\beta$ (the ratio between the final and the initial thickness of the model crust) indicating an absolute decrease in thickness of the model lower crust (Figure 6) [see also *Bonini et al.*, 2001]. The glycerol migration in this case is parallel to the direction of extension and the large accumulations develop preferentially below the footwall of the normal faults bounding the main depression [see also *Bonini et al.*, 2001], although sub-horizontal glycerol bodies were also isolated beneath the main rift depression (Figure 5a).

[20] Conversely, in model NRTZ5 ($\phi = 90°$, Figure 5b) almost all of the glycerol accumulated above the initial reservoir, at the core of a prominent WLC dome, referred to as the "central dome" (CD), which developed within the transfer zone. In this case, the final pattern of doming and emplacement suggests that the glycerol flowed mainly in a direction perpendicular to the extension direction. The patterns of lower crust doming and experimental magma emplacement suggest that faulting in the brittle crust has a strong influence on the migration and accumulation of ductile materials. The process evolves as follows.

[21] The presence of the weak lower crust and experimental magma reservoir favors localization of deformation within the transfer zone; strain localization, in turn, facilitates the propagation and linkage of two border fault segments of opposite dip [e.g., *Ebinger et al.*, 1989], accommodating most of the deformation and generating a sharp decrease in the vertical pressure exerted on both the experimental lower crust and magma below the grabens; following this pressure drop, ductile materials flow toward the transfer zone and the experimental magma is transferred laterally in a rift-parallel direction.

[22] The different patterns of magma migration and the final arrangement of the intrusions suggest that it is the style of the deformation, controlled by the angle ϕ, that has the strongest influence on the modalities of ductile material migration. In the following sections we analyze these processes by calculating the pressure differences and related buoyancy forces occurring in the models as a result of faulting in the brittle crust, and which are responsible for the lateral flow of lower crust and magma.

4. Dynamics of Magma Migration

[23] Heterogeneous thinning of the lithosphere generates lateral pressure differences, which in turn trigger a lateral flow of ductile materials that tends to bring the lithosphere into a laterally homogeneous and vertically stable state [e.g., *Artyushkov*, 1973]. The flow of ductile materials is controlled by the horizontal force per unit length exerted by one lithospheric column onto another (buoyancy force, F_b [e.g., *Fleitout and Froidevaux*, 1982; *Buck*, 1991; *Stüwe and*

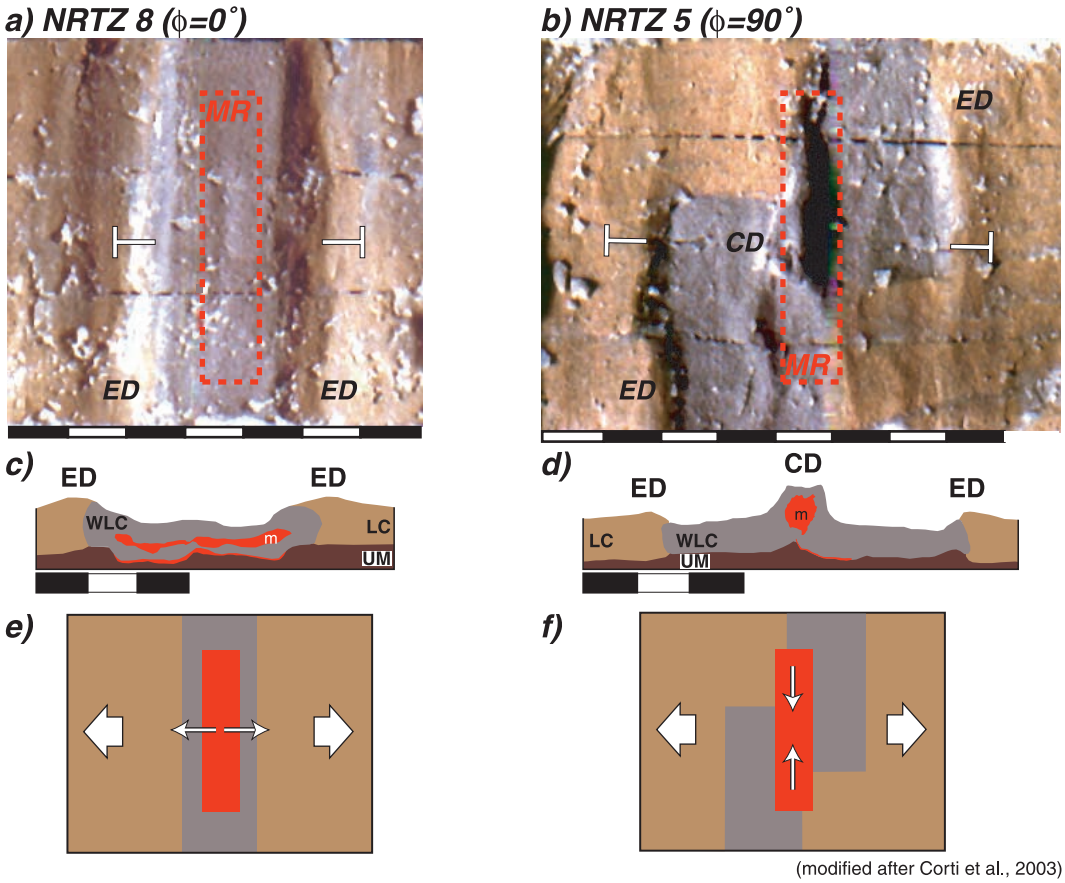

Figure 5. (a–b) Top view photos (light is from left to right) showing the pattern of ductile doming in models NRTZ8 (a) and NRTZ5 (b). The photographs were taken after removal of the upper sand layer; the dashed rectangular box in the top view indicates the initial position of the experimental magma reservoir (MR). (c–d) Line drawings of cross sections through ductile materials showing the lateral flow of magma in model NRTZ8 (c), and magma emplacement corresponding to the Central Dome in model NRTZ5 (d). The main flow trajectories hypothesized for models (e) NRTZ8 and (f) NRTZ5 are also indicated. CD: Central Dome; ED: External Dome. Other symbols as in Figure 1. Scales are in centimeters. Modified after *Corti et al.* [2003] (with permission from Elsevier Science).

Barr, 2000, and references therein]. This force reflects a difference in the gravitational potential energy, which is mainly related to the deflection in density interfaces represented in our experiments by (1) the topography of the model surface, (2) the brittle-ductile interface, and (c) the experimental Moho [e.g., *Ter Voorde et al.*, 1998]. The new distribution of mass results in a pressure distribution expressed, in the case of isostatic compensation, by

$$P(z) = g\int_0^z \rho(s)ds, \tag{1}$$

where g is the gravity acceleration, ρ is the density, and s is the depth varying between 0 and z. The related pressure difference is given by

$$\Delta P(z) = P_A(z) - P_B(z) = g\left[\int_0^z \rho_A(s)ds - \int_0^z \rho_B(s)ds\right], \tag{2}$$

where A and B refer to two different points within the model. Integration of the pressure difference with depth gives the buoyancy force (F_b) [e.g., *Fleitout and Froidevaux*, 1982; *Buck*, 1991; *Stüwe and Barr*, 2000]:

$$F_b = \int_0^{z_C} \Delta P(z)dz = \int_0^{z_C} P_A(z)dz - \int_0^{z_C} P_B(z)dz$$
$$= g\left[\int_0^{z_C}\int_0^z \rho_A(s)dsdz - \int_0^{z_C}\int_0^z \rho_B(s)dsdz\right], \tag{3}$$

where z_C represents the compensation depth. In our experiments, the model upper lithospheric mantle rests directly on a basal rigid plate (the base of the Plexiglas box), so we only simulated the upper part of the continental lithosphere and the dynamics of model deformation did not account for the isostatic compensation provided by the asthenosphere. As a consequence, depth z_C refers to the base of the model, and the patterns of subsidence and extension-induced pressure differences (and related buoyancy forces) are restricted to mass redistribution in the upper lithospheric column.

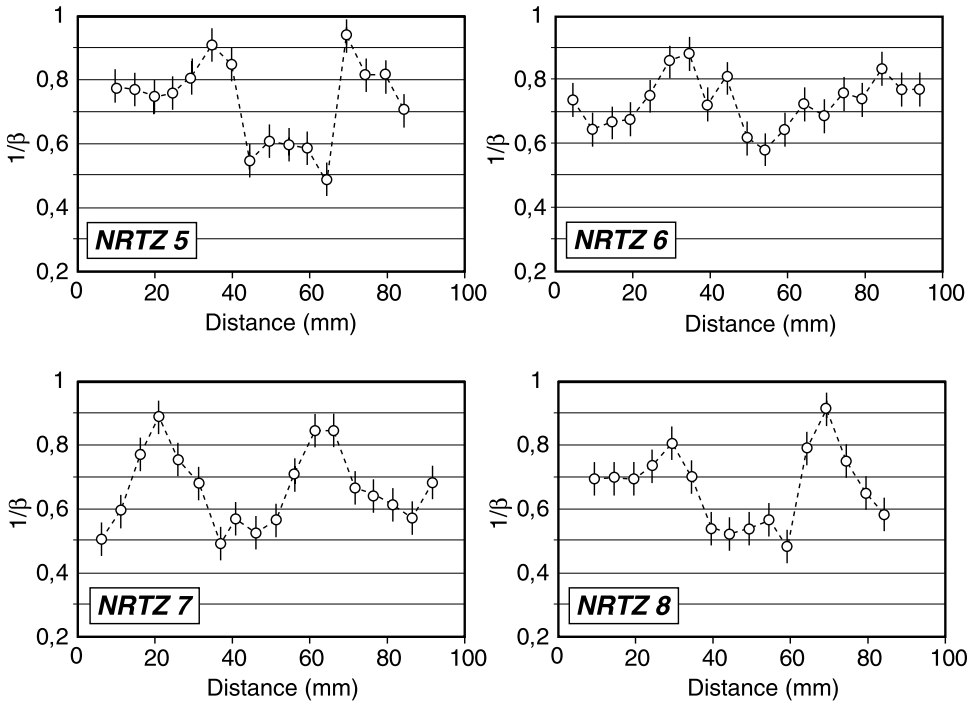

Figure 6. Diagrams showing the thinning factor 1/β (the ratio between the final and the initial layer thickness) for the model lower crust plotted against distance along the cross sections showed in Figure 2. Note the general absolute thinning of the lower crust (1/β < 1) along all the profiles and the relative thickening (indicated by higher 1/β values) corresponding to the ductile domes.

[24] The integral in equation (3) corresponds, in a P versus z graph, to the difference between the areas of the two P-z curves corresponding to two lithospheric columns 1 and 2 within the model [e.g., *Buck*, 1991; *Stüwe and Barr*, 2000; *Davis and Kusznir*, 2002] (Figure 7). Each of these P-z curve areas can be calculated, in the case of a three-layer model lithosphere, as follows:

$$\text{Area} = g\left[\frac{\rho_1 h_1^2}{2} + \frac{\rho_2 h_2^2}{2} + \rho_1 h_1 h_2 + \frac{\rho_3 h_3^2}{2} + (\rho_1 h_1 + \rho_2 h_2) h_3\right] = \int_0^{z_B} P(z)dz, \quad (4)$$

where subscripts 1, 2, and 3 refer to brittle crust, ductile crust and upper mantle, respectively.

[25] Once the P-z curves relative to columns 1 and 2 within the model have been drawn, the buoyancy force (F_b) in equation (3) can be calculated as the difference between the two areas obtained from equation (4):

$$F_b = \text{Area}_1 - \text{Area}_2. \quad (5)$$

[26] In the current experiments, the extension-induced buoyancy forces (F_b) are generated in the central part of the models by thinning of the analogue continental crust associated with the rift depression. As a consequence, forces F_b are directed toward the central part of the model (i.e., riftward; Figure 7a). In the following sections, we show how the patterns of ductile materials migration are controlled by the feedback between the thinning of model lithosphere induced by far-field stresses and the local buoyancy flows induced by the heterogeneous extension [e.g., *Zeyen et al.*, 1996; *Burov and Cloetingh*, 1997; *Huismans et al.*, 2001; *Mulugeta and Ghebreab*, 2001].

4.1. Pressure Differences Acting on the Models

[27] Our analysis of the pressure exerted on models NRTZ5 and NRTZ8 at the beginning and end of deformation is shown in Figure 8. The diagrams show that a low-pressure area characterizes the central part of the model at the onset of deformation, due to the presence of a weak lower crust and low-density experimental magma body (Figure 8). At the end of deformation, the heterogeneous thinning of the models generates a strong lateral pressure gradient. In model NRTZ8 in particular, two low-pressure areas correspond to the two ductile external domes (ED) that formed beside the initial reservoir. Development of the large topographically depressed area, corresponding to the main rift zone, implies that pressure in the central part of the model is smaller than in the flanks of the rift (Figures 8a and 8b).

[28] Pressure distribution is more complex in model NRTZ5, reflecting the greater complexity of the surface

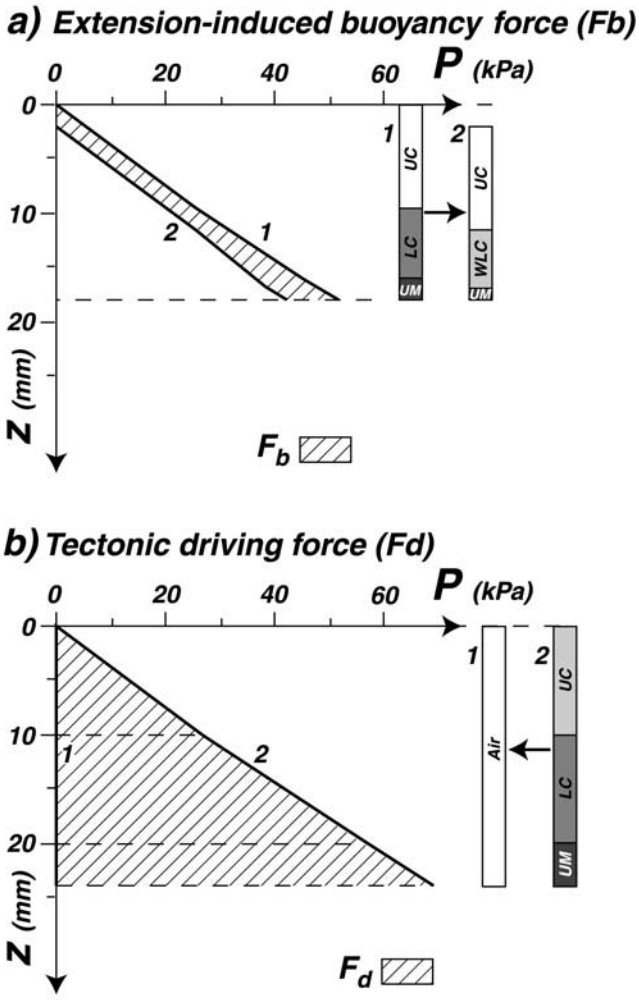

Figure 7. Diagrams of vertical pressure (P) versus depth (z) used to calculate the forces acting in the models. The integrated pressure difference with depth (i.e., the buoyancy force) is indicated by the hachured regions on the graphs, corresponding to the difference between the areas below the P-z curves of two lithospheric columns. The pressure difference between two different points within the model gives rise to the extension-induced buoyancy force, F_b (a), whereas the pressure difference between the model lithosphere (curve and column 1) and the void at the model boundaries (curve and column 2) gives the far-field forces driving extension and thinning of ductile materials, F_d (b).

fault pattern (Figures 8c and 8d). Two relatively low-pressure areas correspond to the two external ductile domes (ED), related to faults orthogonal to the extension direction (Figure 8c). However, the minimum pressure is associated with the central dome (CD) that formed along the transfer zone, which is also the site of major experimental magma accumulation (Figure 8c). The pressure drop associated with the central dome can also be observed in a profile orthogonal to the extension direction (Figure 8d). Obviously, this pressure distribution has important implications on the modalities of magma migration.

4.2. Dynamics of Experimental Magma and Lower Crust Flow

4.2.1. Model NRTZ8, $\phi = 0°$ (Single Rift Segment)

[29] As stated in section 2.1, extension of the multilayer system was achieved by lateral expansion of the models in response to the centrifugal body force field simulating gravity in nature. Outward-directed migration (i.e., thinning) of the ductile layers transmitted stresses to the overlying brittle layer that faulted in correspondence of the weakest regions of the model (i.e., at the pre-defined weakness zones; Figure 9). In particular, deformation was localized in the central part of the models, because the weakest region of the laterally inhomogeneous model lower crust stretched and thinned faster than the stronger margins (Figure 9). From a mechanical perspective, this simulates a necking instability in the extending lithosphere [e.g., *Mulugeta and Ghebreab*, 2001].

[30] Model dynamics was primarily controlled by the pressure difference between the model lithosphere and the void at the free model boundaries [e.g., *Mulugeta and Ghebreab*, 2001], which may be considered analogous to the thinning induced by the far-field extensional forces (F_d) in nature [e.g., *Zeyen et al.*, 1996; *Huismans et al.*, 2001] (Figures 7b, 9a, 10a, and 10b). Extension-induced buoyancy forces due to crustal thinning (F_b) acted in an opposite direction and tended to drive an inward-directed flow (thickening) of ductile material, trying to restore the pressure imbalance (Figures 9a, 10a, and 10b). During extension, the stress differences inducing the far-field thinning were higher than the inward-directed buoyancy forces resulting in an outward flow of ductile materials and absolute thinning of the ductile layers (Figure 9b). In these conditions, the experimental magma moved laterally toward the margins of the deformed zone. Owing to its low viscosity, glycerol migrated faster then the surrounding ductile materials. These above results are consistent with analogue models by *Mulugeta and Ghebreab* [2001], showing that pressure gradients at the margins of the model drive material flow outward even when the pressure is lower in the axial part of the model. When the far-field extensional forces, are no longer active in this process (i.e., extension ceases or is greatly reduced), than the lower crustal material tends to flow inward from the sides of the rift zones initiating a convergent flow toward the central depression [e.g., *Mulugeta and Ghebreab*, 2001]. The process may also lead to the post-rift compression suggested by numerical models [e.g., *Burov and Cloetingh*, 1997; *Huismans et al.*, 2001]. Gravity-driven crustal shortening has also been proposed to occur after rift cessation in natural failed rifts [e.g., *Knott*, 2001].

[31] Notably, during extension the deformation is localized beside the initial reservoir and movement on normal faults generates local pressure differences between these areas of heterogeneously thinned upper crust and the thicker surrounding regions (i.e., the marginal grabens and the rift flanks, respectively; Appendix B). The related forces ($F_{b\mathrm{ED}}$)

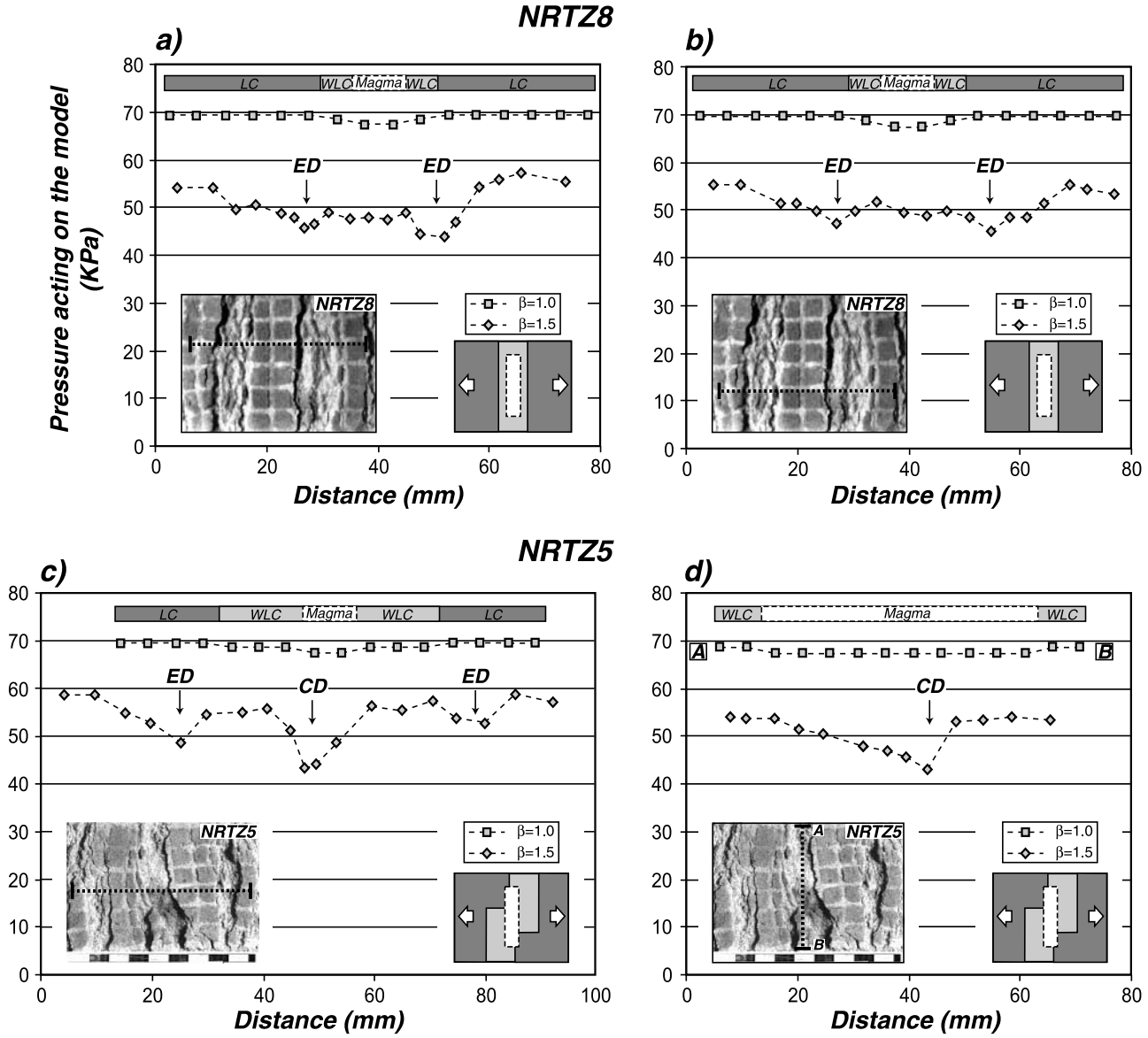

Figure 8. Pressure at the base of models along two different profiles in each NRTZ8 (a–b) and NRTZ5 (c–d) experiment, calculated at the onset (β = 1.0) and at the end (β = 1.5) of deformation. Symbols as in Figures 2 and 5.

enhance the lateral ductile migration and promote a relative flow of ductile materials that leads to local relative thickening at the external domes (ED), as well as the lateral transport of experimental magma toward the core of the domes (Figures 9 and 10a). This also determines that the inferred trajectories of experimental magma migration are almost horizontal below the main rift depression and become oblique (and possibly vertical) below the ductile dome regions (see the cross-section in Figure 5a), implying the development of the marginal grabens controls the experimental magma ascent. Once the interface between the low-density glycerol and the overlying brittle layer has been sufficiently displaced, the buoyancy force related to this density contrast can drive further diapiric deformation.

[32] Finally, it is worth noting that, due to the lateral density variation, the less dense WLC tends to intrude the denser LC during the lateral migration and doming process (Figure 10a).

4.2.2. Model NRTZ5, $\phi = 90°$ (Offset Rift Segments)

[33] As in model NRTZ8, deformation of the system is controlled by the interaction between the far-field thinning of model lithosphere and the local buoyancy forces related to the heterogeneous stretching. Away from the transfer zone, ductile materials still flow laterally to form ductile domes at the LC-WLC rheological boundaries, driven by minor pressure differences (Figures 10c and 10d). During deformation of model NRTZ5, however, overlapping at the transfer zone of two opposite border fault systems leads to the

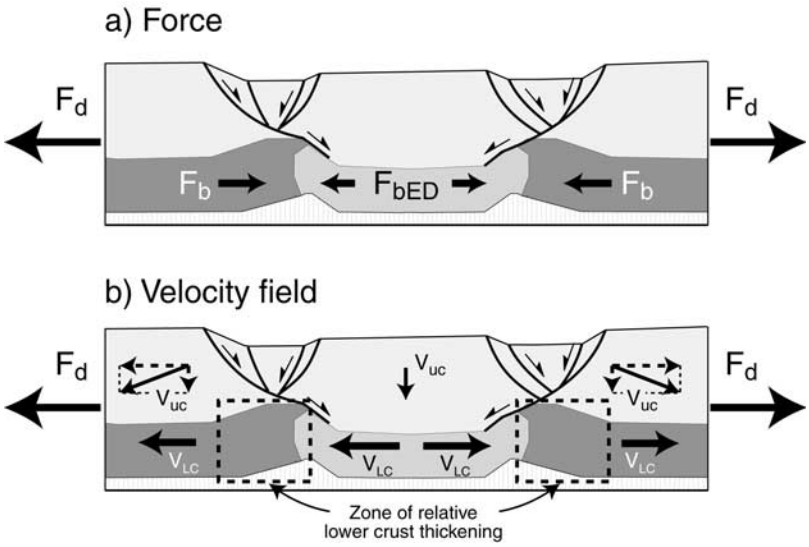

Figure 9. Schematic representation of the dynamics of ductile materials migration based on model NRTZ8. (a) Forces acting in the system. F_d indicates the far-field forces driving extension and the thinning of ductile materials observed in the models (see Figure 6). Within the model, heterogeneous thinning of the upper crust creates inward-directed buoyancy forces (F_b) and outward-directed forces (F_{bED}) related to unloading that correspond to the marginal grabens. (b) Representation of the velocities within the different model crustal blocks. The magnitude of the velocity vectors is qualitative. In the upper crust, the block within the central depression is subjected to almost pure subsidence, whereas the blocks corresponding to the rift shoulder are mainly driven apart and subjected to a prevailing horizontal movement. The whole lower crust is thinned and thus subject to an outward migration. Maximum deformation rates occur below the rift depression and corresponding with the weak lower crust, as indicated by the highest thinning factor in this region (see Figure 6). Lower velocities are observed in the normal lower crust below the rift flanks; this velocity gradient gives rise to the relative thickening observed below the marginal grabens [e.g., *Zeyen et al.*, 1996]. This difference in velocities also determines that the weak lower crust intrudes the normal lower crust.

development of a buoyancy force, F_{bCD}, acting also in an extension-orthogonal (rift-parallel) direction (Appendix B). The effect of this force dominates over the far-field thinning, inhibiting the lateral outward flow of glycerol and triggering its migration inward toward the CD forming at the transfer zone (Figure 10c). thus the experimental magma transfer trajectories are predominantly orthogonal to the extension direction and parallel to the main rift axis as well as the trend of the initial reservoir (Figures 5b and 10c). As deformation continues, the accumulation of magma at the CD core further decreases the pressure, leading to an even greater mass of ductile materials at the dome region and possibly promoting a feedback interaction.

5. Discussion and Comparison With Nature

[34] The experiments have shown that deformation of the model lithosphere, which is governed by the geometry of inherited structures, plays a major role in controlling the flow patterns of ductile materials, such as the experimental lower crust and magma. In response to extension, faulting in the brittle crust drastically reduces the pressure exerted on the ductile materials, generating lateral pressure gradients that force them to flow toward low-pressure regions [e.g., *Brune and Ellis*, 1997]. Thus extension promotes a "reactive" migration of ductile materials, as pointed out by *Jackson and Vendeville* [1994].

[35] Analysis of pressure differences and buoyancy forces suggests that deformation of ductile materials is mainly controlled by the feedback between thinning of model lithosphere induced by far-field forces and the local buoyancy flows induced by the heterogeneous extension [e.g., *Huismans et al.*, 2001]. In the general case of a single main rift development, the first effect dominates, promoting a lateral outward-directed migration of experimental magma and lower crust from their initial central position. Local forces (F_{bED}) related to unloading of the marginal grabens enhance the lateral ductile migration and, coupled to the low viscosity of the weak lower crust, determine lateral variations in the velocity of outward migration, with the central part of the models thinning (and migrating) faster than the shoulders (Figure 9b). This results in the relative thickening of ductile materials at the margins of the deformation zone and development of external domes. Similar results have been obtained in previous numerical models documenting

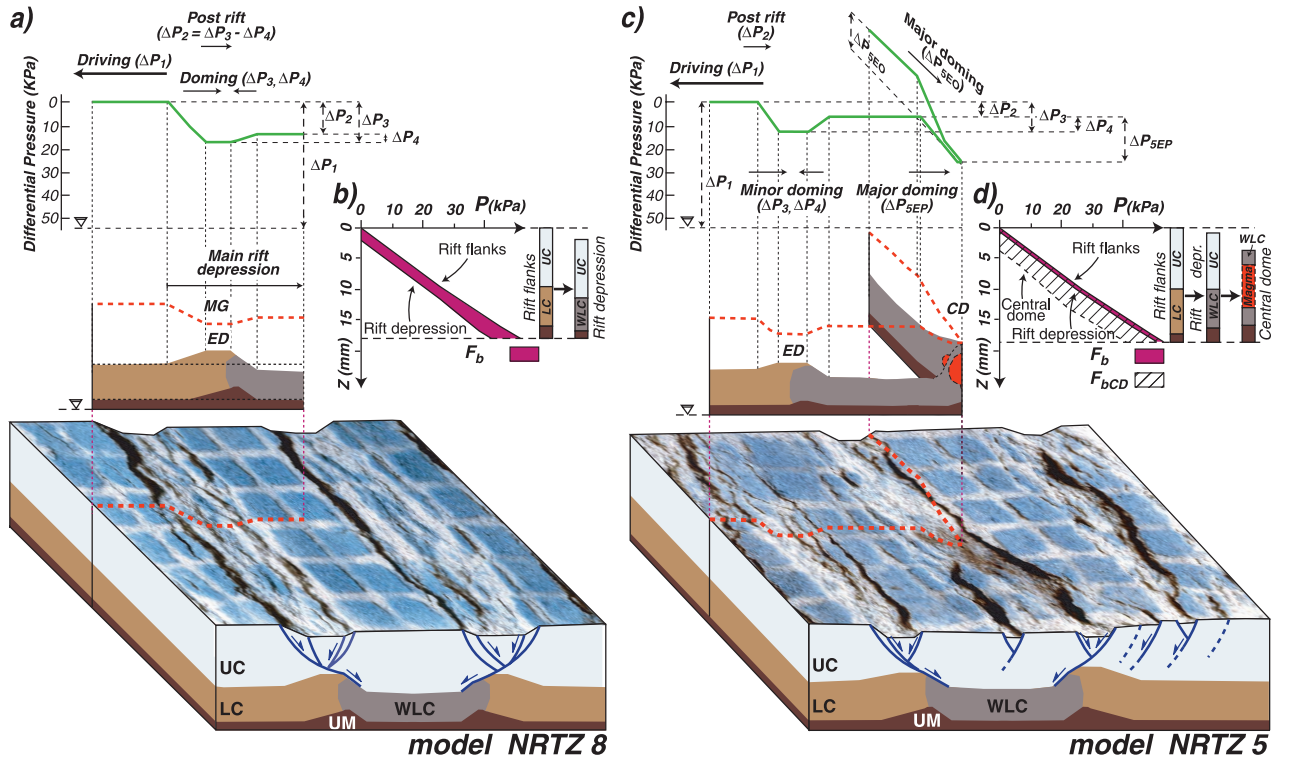

Figure 10. Schematic block diagrams and pressure(P)-depth(z) graphs showing the main pressure differences (and related forces) acting on models NRTZ8 (a–b) and NRTZ5 (c–d). (a) Differential pressures exerted in model NRTZ8. (b) P-z graph for two material columns located on the rift flanks and within the main rift depression. The difference in pressure between the two columns gives rise to the extension-induced buoyancy force, referred to as F_b in the text and indicated by the purple region in the graph. (c) Main differential pressures acting on model NRTZ5. Note the two different components of the pressure difference ΔP_5, activated along both an extension-parallel (ΔP_{5EP}) and extension-orthogonal (ΔP_{5EO}) direction (see Appendix B for details). (d) P-z graph showing the buoyancy forces generated by the pressure difference between the rift flanks and the main rift depression (F_b) and between the main rift depression and the central dome region (F_{bCD}). Other symbols as in Figures 2 and 8.

that the relative ductile thickening corresponding to the rift shoulders is promoted by the outward migration of the lower crust with velocities decreasing from the rift depression outward [*Zeyen et al.*, 1996]. Development of the external dome also determines that the inferred trajectories of magma migration change from almost horizontal below the main rift depression to oblique (and possibly vertical) below the ductile domes. Numerical models have shown that at least three other main processes may enhance the outward migration of magma and favor its emplacement coincident with, or below, the rift margins: (1) modification of the strain field in response to the development of large boundary faults [*Ellis and King*, 1991] (see below section 5.2); (2) buoyancy forces associated with lithospheric mantle thinning, Moho uplift and possible dynamic pressures due to upwelling of the asthenosphere beneath the basin (i.e., the rift-push concept) [e.g., *Huismans et al.*, 2001; *Davis and Kusznir*, 2002] and (3) pressure gradients generated by subsidence (and sedimentation) within the rift depression and uplift (and erosion) of the shoulders [*Burov and Cloetingh*, 1997]. Additionally, strong sedimentation in the main depression (not included in the current modeling) may further increase the lateral magma transfer by reducing the local pressure drop related to the development of marginal grabens by shifting the trajectories of migration from horizontal to sub-vertical.

[36] The lateral migration of ductile materials may represent an important process during continental rifting, and may account for the greater thinning of the lower crustal relative to the upper crust that is observed in many seismic profiles, and for the thickening of ductile materials beneath the rift shoulders (the ED in this study) leading to the uplift of the rift flanks, documented in many extensional areas worldwide [e.g., *Zeyen et al.*, 1996, and references therein].

[37] On the other hand, a transfer zone accomplishing deformation between two rift segments leads instead to a pressure drop and associated buoyancy forces (F_{bCD}) that are activated in an extension-orthogonal direction. These forces dominates over the far-field thinning, driving the magma and the weak lower crust toward the transfer zone itself. In this case, the development of the external domes is reduced considerably and, given the initial asymmetric

geometry of the magma reservoir, the magma begins to migrate in a direction orthogonal to that of extension.

[38] Before comparing the modeling results with nature we discuss the main limitations characterizing our experimental approach.

5.1. Limitations of the Models

[39] Continental rifting is a thermo-mechanical process in which temperature-dependent processes such as crystallization-melting and variations in magma rheology or thermal weakening of the country rocks represent first-order factors controlling the evolution of deformation and its relations with the dynamics of magma migration. Thus the main limitations of the current modeling are mainly related to the rheology of the experimental materials, and to the experimental approach with which we simplified continental extension to an isothermal (purely mechanical) process.

[40] Important simplifications have been applied to the rheological characteristics of the magma analogue (glycerol) that, when scaled to nature, is only able to simulate a high viscosity magma (of the order of 10^{16} Pa s). However, the glycerol is 5 orders of magnitude less viscous than the model lower crust, implying that this material is still suitable to model a significant viscosity contrast between the low-viscosity melt fraction and the host rocks [*Cruden et al.*, 1995]. Notably, the lower viscosity contrast between the glycerol and the lower crust with respect to nature allowed the model magma to rise in a predominantly diapiric way [e.g., *Ramberg*, 1971], thus simplifying the complex mechanisms of magma transfer within the continental crust [e.g., *Petford et al.*, 2000] (see section 5.2).

[41] In extrapolating the experimental results to nature, we have also implicitly assumed that the bulk of the underplated magma does not freeze quickly in place below the crust but migrates a significant distance before solidifying (see section 5.2). This is a valid approximation for natural conditions, as the thermal anomalies in actively deforming regions (either generated by thinning of the lithosphere or by conduction from plume materials) are likely to give rise to repeated intrusions of basalt into the underplated layer, hindering its solidification and providing extra heat for partial melting of the lowermost crust [*Cruden et al.*, 1995, and references therein].

[42] Thus, as discussed by *Bonini et al.* [2001] and *Corti et al.* [2003], we consider the present analogue simulations to be valid despite the above mentioned simplifications, because our investigations were focused exclusively on the interactions between deformation and magma migration during continental lithospheric extension.

5.2. Comparison With Nature

[43] The dynamics of the two end member processes of magma migration described above may have relevance to the understanding of the tectonic and volcanic setting of the Main Ethiopian Rift, and of the Western Branch in the East African Rift System (Figure 11).

[44] In the Main Ethiopian Rift, which may be viewed as a single rift segment, several off-axis volcanoes formed during the Pliocene on the rift shoulders, in a position external to the normal faults bordering the rift depression. Previous studies interpreted the off-axis volcanism in the Main Ethiopian Rift as the result of the reactivation of pre-existing weakness zones [*Mohr and Potter*, 1976], the outward flow of basaltic melts from magma chambers below the subsiding rift [*Kazmin et al.*, 1980], or a combination of these two mechanisms (i.e., lateral migration of magma coupled with ascent through reactivated old boundary faults) [*WoldeGabriel et al.*, 1999]. Our models suggest that the lateral migration of magma in a direction that is nearly parallel to the regional extensional direction may be responsible for the development of a large number of volcanic edifices on the rift shoulders during Pliocene times [*Kazmin et al.*, 1980; *Bonini et al.*, 2001; *Corti et al.*, 2003] (Figure 11a). The rift-push due to asthenosphere upwelling coupled with subsidence/sedimentation in the rift depression and uplift/erosion of the shoulders may have enhanced the lateral migration of magma. During this process large volumes of magma may have accumulated below the rift shoulders where the dilational strain field developing in the footwall of normal faults could facilitate the ascent of molten materials to feed the off-axis volcanoes [*Ellis and King*, 1991]. This hypothesis is supported by the negative residual gravity anomalies that coincide with the position of the off-axis volcanoes, indicating the presence of magma at depth [*Mahatsente et al.*, 1999].

[45] In the Western Branch, the main volcanic provinces show a close spatial association with major transfer zones [*Rosendahl*, 1987; *Ebinger*, 1989a, 1989b] (Figure 11b). Field studies have shown that the transfer zones are generally associated with pre-rift lithospheric structures as polarity reversals between adjacent rift segments occur predominantly at the intersections between pre-existing fabrics with different trends [*Versfelt and Rosendahl*, 1989]. Geochronology analysis has further documented that magmatic bodies may be present from the earliest stages of extension and may play an important role in the evolution of deformation [*Ebinger*, 1989a, 1989b; *Ebinger et al.*, 1989]. Indeed, *Ebinger et al.* [1989] have suggested that a strong interaction takes place between magmatism and deformation at transfer zones: on one hand, magmatic processes facilitate (but are not a prerequisite for) propagation and linkage of en echelon border fault segments, thus possibly influencing the along-axis segmentation of continental rifts. On the other hand, volcanic activity at transfer zones is favored by the presence of steep border fault tips and transfer faults, as well as by the close spacing of faults within the transfer zone itself. Our models suggest that the concentration of magmatic activity at transfer zones may be directly related to the along-axis migration of magma in response to pressure differences arising from the necking of the brittle crust, inducing a major accumulation of magma beneath these structures (Figure 11b). As suggested by *Ebinger et al.* [1989], once magma is collected at these structures, volcanic

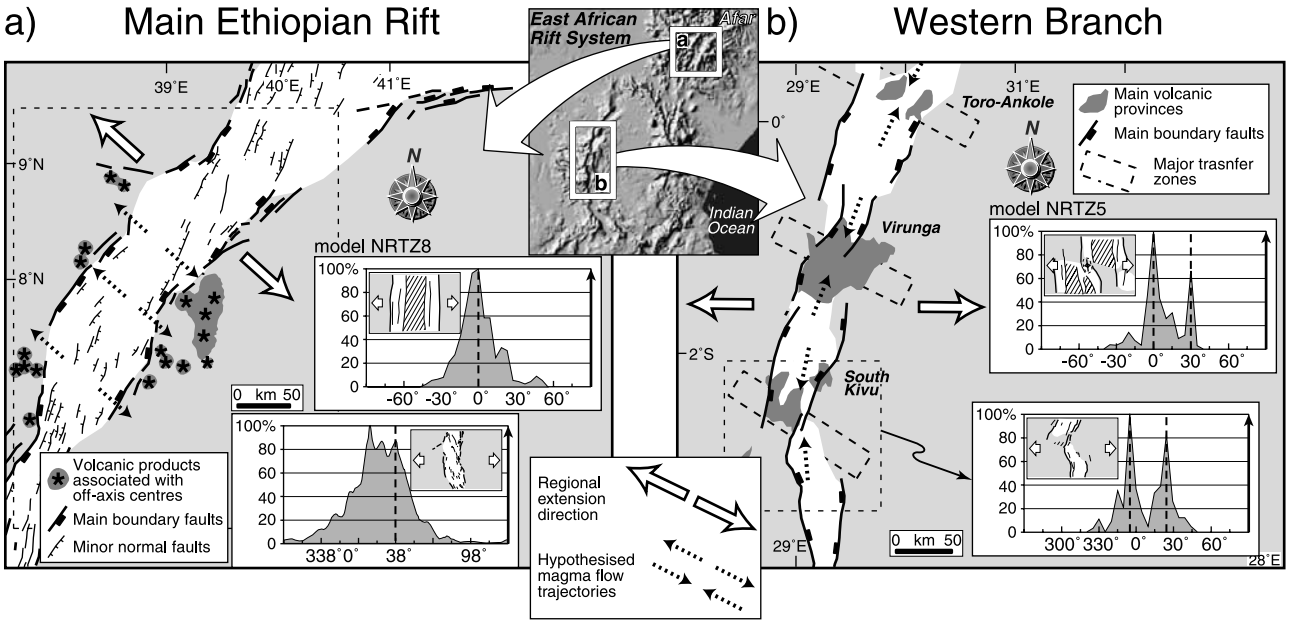

Figure 11. Extrapolation of the dynamics of magma migration to natural examples. Application (a) of model NRTZ8 results to the Main Ethiopian Rift and (b) model NRTZ5 results to the Western Branch of the East African Rift System. In our interpretation, the lateral outward flow of ductile materials is responsible for the development of off-axis volcanoes in the Main Ethiopian Rift (a), whereas rift-parallel magma migration is able to explain the localization of volcanic activity at transfer zones in the Western Branch (b). Comparison of models results with nature is implemented by the comparison between statistical analysis (histograms) of fault distribution (fault pattern in (a) simplified after *Corti et al.* [2001] (with permission from Elsevier Science) and that in (b) after *Rosendahl* [1987] (reprinted, with permission, from *Annual Review and Planetary Sciences* (www.annualreviews.org)) and *Ebinger* [1989a, 1989b]). The black arrows in the graphs indicate the bulk stretching directions [see also *Bonini et al.*, 1997; *Corti et al.*, 2001] regional extension direction in the Western Branch is assumed to be roughly E-W [e.g., *Daly et al.*, 1989; *Ebinger*, 1989a, 1989b]. The remarkable similarity of the histograms indicates a marked similarity in the structural pattern between experiments and nature. Note that the maximum peak at N20° in the histogram of structures in the Main Ethiopian Rift represents faulting in a later stage (Quaternary) of oblique rifting [*Bonini et al.*, 1997; *Corti et al.*, 2001]. Symbols as in Figure 10.

activity may be favored by the presence of subvertical oblique-slip transfer faults that provide ready conduits for the ascent of magma to the surface. Indeed, since the pressure required to penetrate fractures is (for a given depth) a function of the fracture dip, these oblique slip faults require the lowest pressure to be penetrated [*Acocella et al.*, 1999b; *Corti et al.*, 2003]. Although we have greatly simplified the rheology of the materials involved in the process, we believe this process of magma migration is largely independent of the composition and viscosity of the magma, and hence unaffected by the mechanism of its ascent through the crust. A low-viscosity magma would respond directly to the regional stress field in the lithosphere by favoring widespread diking, a process that dominates the advanced stages of continental rifting and that results in a uniform distribution of magmatic products along the entire rift structure. However, magmatism is concentrated in the transfer zones especially during the early stages of continental rifting (e.g., the Western Branch of the East African Rift System), suggesting that rift-parallel magma migration is induced by lateral pressure differences, as occurred in our model experiments.

6. Conclusions

[46] Centrifuge models were designed to analyze the dynamic relations between crustal-scale deformation and magma emplacement during rift evolution involving the reactivation of inherited weakness zones in the lower crust. The results support the observation that the geometry of these reactivated weakness zones has a strong influence on the architecture of the rift system. A straight lower crust weakness zone placed in the central part of the model resulted in a single rift segment, while two weak lower crust segments with a right-angle offset generated two main rift segments linked by a transfer zone. Faulting and the related heterogeneous thinning of the upper crust generated buoyancy forces, which in turn controlled the migration of ductile materials (model magma and lower crust). Analysis of the experimental results allowed us to identify two mechanisms of magma migration during rifting.

[47] In the single rift segment, both magma and lower crust are transferred laterally toward the rift flanks, until they reach the region below the marginal grabens where local pressure decreases and the associated forces are able to influence the final collection/emplacement of the magma/ductile crust system.

[48] In distinct rift segments, the development of a transfer zone perturbs the dynamics of magma migration. The pressure drop related to oblique faulting generates an additional force, whose extension-orthogonal component is able to drive magma toward the transfer zone, causing along-rift axis magma migration.

Appendix A: Strength Profiles and Scaling of the Total Strength of the Experimental Lithosphere

[49] Rheological or strength profiles, in which the differential stress ($\sigma_1 - \sigma_3$) is plotted against depth, have been widely used to represent the rheological characteristics of the lithospheric multilayer [e.g., *Ranalli*, 1995]. Integration of the local differential stress with depth gives the strength of the different brittle and ductile layers; in turn, the sum of the single layer strengths give the total strength of the lithosphere (see below).

A1. Brittle Layers

[50] In terms of principal stresses, the governing equation for tensional faulting in Coulombian brittle layers is expressed by

$$(\sigma_1 - \sigma_3) = \frac{2\mu\rho g z(1-\lambda) + 2c_0}{(\mu^2+1)^{1/2}+\mu}, \tag{A1}$$

where c_0 is the cohesion, μ is the internal friction, ρ is the density of the overlying material at depth z, g is the acceleration due to gravity, and λ is the Hubbert-Rubey coefficient of fluid pressure (ratio of water pressure to overburden pressure). For the current experiments λ was calculated to be on the order of $\sim$0.5, such that the critical stress difference at the base of the model upper crust is $\approx 9.4\ 10^3$ Pa (Figure 1e).

A2. Ductile Layers

A2.1. Newtonian Materials

[51] The generalized constitutive equation for Newtonian fluids can be written in the form [e.g., *Ranalli*, 1995]:

$$\sigma_{ij} - p\delta_{ij} = c_{ijkl}\dot{\varepsilon}_{kl}, \tag{A2}$$

where $p = 1/3\ (\sigma_{11} + \sigma_{22} + \sigma_{33})$ is the mean normal stress (component of the total stress that makes no contribution to the strain rates in an incompressible fluid), δ_{ij} is the Kronecker delta or identity matrix ($\delta_{ij} = 1$ for $i = j$, $\delta_{ij} = 0$ for $i \neq j$), c_{ijkl} are the viscosity coefficients, and $\dot{\varepsilon}_{kl}$ are the components of the tensor strain rate defined as

$$\dot{\varepsilon}_{kl} = \frac{1}{2}\left(\frac{\partial v_k}{\partial x_l} + \frac{\partial v_l}{\partial x_k}\right). \tag{A3}$$

Like many geological problems, bulk deformation of models can be reasonably approximated to a two-dimensional problem, such as the stress tensor σ_{ij} can be reduced to four components σ_{11}, σ_{22}, $\sigma_{12} = \sigma_{21}$. For an isotropic, incompressible Newtonian element equation (A2) can be rewritten in the form

$$\sigma'_{11} = \sigma_{11} - \overline{p} = 2\eta\dot{\varepsilon}_{11} \tag{A4a}$$

$$\sigma'_{22} = \sigma_{22} - \overline{p} = 2\eta\dot{\varepsilon}_{22} \tag{A4b}$$

$$\sigma'_{12} = \sigma_{12} = 2\eta\dot{\varepsilon}_{12}. \tag{A4c}$$

In case of pure shear deformation, $\sigma_{12} = 0$ and equation (A2) can be expressed in terms of principal stresses as follows:

$$\sigma_1 - \sigma_3 = 2\eta(\dot{\varepsilon}_1 - \dot{\varepsilon}_3) = 4\eta\dot{\varepsilon}_1 \tag{A5}$$

since $\dot{\varepsilon}_1 = -\dot{\varepsilon}_3$ (strain rates in the longitudinal and vertical directions, respectively) because of incompressibility.

[52] In our models, the mean longitudinal strain rate can be calculated as $\dot{\varepsilon}_1 = \frac{V}{x}$, where x is the actual width of the deformed zone of the model and V is the extension velocity imposed on the models [e.g., *Ramberg*, 1980; *Benes and Davy*, 1996]. Since deformation at the onset of extension is localized and corresponds with the WLC, $\dot{\varepsilon}_1 \approx \frac{2.5 10^{-4}}{210^{-2}} = 1.2\ 10^{-2}\ s^{-1}$ such that the differential stress in the Newtonian glycerol body is $\sim 4.8\ 10^{-2}$ Pa (Figure 1e).

A2.2. Non-Newtonian (Power Law) Materials

[53] Shear experiments for our experimental ductile materials representing the lower crust and upper mantle gave a steady state flow that can be expressed in the form of

$$\dot{\varepsilon}_S = A\sigma_S^n, \tag{A6}$$

where $\dot{\varepsilon}_S$ and σ_S are the shear component of the strain rate and the shear stress, respectively, A is a material parameter which is a function of pressure, temperature and material properties and n is a constant (the stress exponent, $n > 1$). From this experimentally derived equation, the generalized power law creep equation for non-Newtonian fluids can be written in tensor form as follows [e.g., *Ranalli*, 1995]:

$$\dot{\varepsilon}_{ij} = A\sigma_E'^{(n-1)}\sigma'_{ij}, \tag{A7}$$

where σ'_E (effective stress) is given by

$$\sigma'_E = \left(\frac{1}{2}\sigma'_{ij}\sigma'_{ij}\right)^{1/2}. \tag{A8}$$

Table A1. Total Resistance of the Analogue Layers

Analogue Layer	Resistance, Pa m
Upper crust	47
Lower crust	18
Weak lower crust	7
Magma	$9.6\ 10^{-5}$
Upper lithospheric mantle	15
Lithosphere[a]	
A–B	80
C–D	69
E–F	62
G–H	73

[a]Calculated for the strength profiles reported in Figure 1d.

The $\frac{1}{2}\sigma'_{ij}\sigma' = I'_2$ represents the second invariant of the stress deviator, expressed as

$$I_2^{'} = -\left(\sigma'_{11}\sigma'_{22} + \sigma'_{11}\sigma'_{33} + \sigma'_{22}\sigma'_{33}\right) + \sigma'^2_{12} + \sigma'^2_{13} + \sigma'^2_{23}. \quad \text{(A9)}$$

For plane stress (coordinates x_1, x_3), the second invariant reduces to $I'_2 = -(\sigma'_{11}\sigma'_{33}) + \sigma'^2_{13}$. In condition of pure shear $\sigma'^2_{13} = 0$ and

$$I_2^{'} = -\left(\sigma'_{11}\sigma'_{33}\right) = \frac{1}{4}(\sigma_{11} - \sigma_{33})^2. \quad \text{(A10)}$$

Thus, with these assumptions, $\sigma'_E = \frac{1}{2}(\sigma_{11} - \sigma_{33})$ and

$$\dot{\varepsilon}_{ij} = A\frac{1}{2^{(n-1)}}(\sigma_{11} - \sigma_{33})^{(n-1)}\sigma'_{ij}. \quad \text{(A11)}$$

Thus

$$\dot{\varepsilon}_{11} = A\frac{1}{2^{(n-1)}}(\sigma_{11} - \sigma_{33})^{(n-1)}\sigma'_{11} \quad \text{(A12a)}$$

and

$$\dot{\varepsilon}_{22} = -\dot{\varepsilon}_{11} = A\frac{1}{2^{(n-1)}}(\sigma_{11} - \sigma_{33})^{(n-1)}\sigma'_{22} \quad \text{(A12b)}$$

since $\dot{\varepsilon}_{22} = -\dot{\varepsilon}_{11}$ because of incompressibility. Subtracting equation (A12b) from (A12a), and expressing in terms of principal stresses, we obtain

$$(\sigma_1 - \sigma_3) = 2\left(\frac{\dot{\varepsilon}_1}{A}\right)^{(1/n)}. \quad \text{(A13)}$$

This calculation gives, for the experimental strain rate, differential stresses of $1.8\ 10^3$ Pa for the normal lower crust, $7\ 10^2$ Pa for the weak lower crust and $3.6\ 10^3$ Pa for the upper lithospheric mantle (Figure 1e).

A3. Analogue Lithosphere Strength

[54] As stated above, the strength of the single layers is calculated by integrating the differential stress with depth:

$$R_i = \int_{\text{bottom}(i)}^{\text{top}(i)} (\sigma_1 - \sigma_3)(z)dz \quad \text{(A14)}$$

where R represents a force per unit width. In the strength profile, this integral corresponds to the area below the $(\sigma_1 - \sigma_3)$/depth curve. The integrated resistance of the single analogue layers is reported in Table A1.

[55] The total strength of the lithosphere is a measure of the average stress required to extend the lithosphere at a given rate. It is given by the sum of the strength of the single layers:

$$R_L = \sum_i R_i. \quad \text{(A15)}$$

Calculations reported in Table A1 show that the total resistance of our experimental lithosphere varies from 62 Pa m in the weakest regions of the model (above the initial magma reservoir) to 80 Pa m above the rift shoulders.

A4. Dynamic Scaling of Models

[56] Dynamic similarity in the models has been tested by dimensionless ratios relating gravitational stresses to differential stresses in brittle and ductile deformation.

[57] In the ductile layer, the Ramberg number *Rm* [*Weijermars and Schmeling*, 1986] has been calculated as

$$R_m = \frac{\rho g h_d}{(\sigma_1 - \sigma_3)_{\text{viscous}}}. \quad \text{(A16)}$$

The differential stress for viscous deformation in the models has been calculated according to equation (A13), whereas in nature it has been calculated following the power law creep equation [e.g., *Ranalli*, 1995]:

$$(\sigma_1 - \sigma_3) = \left(\frac{\dot{\varepsilon}}{A}\right)^{(1/n)} \exp\left(\frac{E}{nRT}\right), \quad \text{(A17)}$$

where $\dot{\varepsilon}$ is the strain rate, T is the absolute temperature, R is the gas constant (8.31 J mol^{-1} K^{-1}) and A, n and E are the creep parameters of the material. In this calculation we have assumed the power law parameters (A = $3.2\ 10^{-3}$ MPa^{-n} s^{-1}, n = 3.3, E = 268 kJ mol^{-1}) reported by *Fadaie and Ranalli* [1990], investigating the same tectonic setting of our experimental modeling. Given the imposed isothermal behavior of our experimental lower crust, we have assumed an average temperature for this layer by extrapolating the geotherm for the surface heat flow of ~70 mWm^{-2} reported by *Fadaie and Ranalli* [1990] and *Ranalli* [1995] for the Western Branch of the East African Rift System and taking the value corresponding to the middle part of the lower crust. These calculations yield a value of about 50 MPa at ~25 km depth for a natural strain rate of on the order of $5\ 10^{-15}$ s^{-1}. The corresponding value of R_m is 10, which is very close the that determined for the model (R_m = 17, see Table 3). From both natural and model strain rates, the velocity scaling ratio is obtained as $V^* = \dot{\varepsilon}^* h^* = 1.3\ 10^6$, giving scaled natural velocity of ~6 mm/yr.

[58] For the brittle deformation, the dimensionless ratio of stresses was calculated as

$$R_s = \frac{\rho g h_b}{(\sigma_1 - \sigma_3)_{\text{brittle}}}. \quad \text{(A18)}$$

The differential stress at the base of the brittle layer has been calculated using equation (A1). In nature, hydrostatic pore

pressure conditions ($\lambda = 0.42$) and Byerlee's parameters for depth higher than 8 km ($\mu = 0.6$, $c_0 = 60$ MPa) has been considered yielding a differential stress at depths of the brittle/ductile transition of ~250 MPa.

[59] The very close values of R_m and Rs for both models and nature (Table 3) support the dynamic similarity of our analogue experimental approach.

A5. Scaling of the Lithosphere Strength

[60] The reliability of analogue models can be further tested by scaling the total resistance of the analogue lithosphere in the model to nature. Since the integrated resistance has the dimensions of a pressure by a length, the scaling factor can be obtained by assuming that

$$R^* = \frac{R_m}{R_n} = \sigma^* h^*, \tag{A19}$$

where subscript m and n refer to model and nature, respectively.

[61] For the current models, the length-scaling factor ($h^* \approx 5.5 \times 10^{-7}$), together with the model-to-nature ratios of density ($\rho^* \approx 0.5$) and gravity ($g^* = g_m/g_n = 200$), dictate a ratio of normal stress of

$$\sigma^* = \rho^* g^* h^* = 5.5 \times 10^{-5} \tag{A20}$$

such that

$$R^* = 3 \times 10^{-11}. \tag{A21}$$

From equation (A21), the total resistance of the lithosphere R_L, scaled from models to nature, can be estimated to vary between 2.1×10^{12} Pa m (for the weakest regions corresponding to the underplated magma) and 2.7×10^{12} Pa m (for the rift shoulder regions).

[62] This resistance is necessarily lower than the forces driving extension, which can be scaled to nature (from equations (3) and (A18)) yielding values between 2.7×10^{13} Pa m (for the initial configuration) and 1.5×10^{13} Pa m (for a thinned lithosphere at the end of extension). In nature, the resistance of the continental lithosphere undergoing extension varies between 10^{12} Pa m (for high Moho temperatures and no brittle mantle) and 5×10^{13} Pa m (for low Moho temperatures) [e.g., *England*, 1983; *Lynch and Morgan*, 1987; *Davy and Cobbold*, 1991; *Ranalli*, 1995; *Jones et al.*, 1996; *Townsend and Sonder*, 2001]. Since our models were intended to investigate natural conditions characterized by a relatively hot Moho and a ductile upper mantle, the estimate of the scaled lithospheric strength (R_L), which is in the range of natural values, represents a good approximation for the rheological characteristics of an extending continental lithosphere in nature.

Appendix B: Details of Calculations of Differential Pressures and Associated Buoyancy Forces in the Models

[63] The total pressure difference acting on the lower crust and driving the horizontal flow is the sum of the upper crustal and mantle components [e.g., *Ter Voorde et al.*, 1998]. Calculations of differential pressures (and associated buoyancy forces) in our models (Figure 10) have been performed by assuming the model lithospheric column at the rift flank as the reference (undeformed) lithosphere ($\Delta P = 0$) and by analyzing the deflection in density interfaces (i.e., the surface of the model, the brittle-ductile transition and the experimental Moho) in relation to this "standard" configuration.

B1. Model NRTZ8

[64] Because the free expansion of the model was allowed by removing slices of plasticine, the pressure difference at the lateral edges is

$$\Delta P_1 = P_{(\text{model})} - P_{(\text{air})} \approx P_{(\text{model})} \tag{B1}$$

such that ΔP_1 varies between 70 kPa at the onset of deformation to about 55 kPa at the end of deformation (Figure 10a). The related far-field force (F_d) varies between 8×10^2 Pa m and 4.4×10^2 Pa m at the model boundaries and drives deformation of the multilayer system. The pressure differences related to the thinning of the analogue crust, $\Delta P_2 - \Delta P_4$ in Figure 10a, show maximum values in the order of ≈10 kPa, whereas the related extension-induced buoyancy force (F_b) is $\approx 10^2$ Pa m. In order to calculate the buoyancy forces exerted on the model, we chose to integrate ΔP_2 with depth since it is representative of the pressure difference between the rift flanks and the main rift depression (Figure 10a). In this sense, ΔP_2 represents the pressure difference that leads to post-rift deformation (Figure 10a). ΔP_3 represents instead the local pressure difference between the rift flanks and the marginal grabens above the ductile dome; its difference in magnitude with respect to ΔP_2 (that is $\Delta P_4 = \Delta P_3 - \Delta P_2$) is expected to be compensated soon after the end of extension. The pressure difference ΔP_4 and the related buoyancy forces ($F_{b\text{ED}}$) are outward-directed and enhance lateral migration of ductile materials and their relative thickening at the external domes. Since $\Delta P_3 > \Delta P_4$, the shape of the rising lower crust dome(s) is expected to be asymmetric. This is illustrated in Figures 2a and 10a, where domes consisting of both lower crust and upper mantle materials verge toward the center of the main rift depression.

B2. Model NRTZ5

[65] The general picture of deformation is similar to model NRTZ8, and thinning of the experimental crust is, away from the transfer zone, still controlled by the far-field stress. Minor pressure differences, such as ΔP_3 and ΔP_4 in Figure 10c, still drive a formation of ductile domes at the LC-WLC rheological boundaries. During deformation of model NRTZ5, however, an additional pressure gradient (ΔP_5) is generated by overlapping at the transfer zone of opposite border fault systems and subsequent necking of the brittle crust. This pressure difference, which is active in both an extension-parallel ($\Delta P_{5\text{EP}}$) and extension-orthogonal ($\Delta P_{5\text{EO}}$) direction, triggers the migration

of magma and of the weak lower crust toward the CD (Figure 10c). Both components of ΔP_5 share similar values, which are higher than ΔP_3 and ΔP_4. The ΔP_5-related buoyancy force, $F_{bCD} \approx 1.5 \times 10^2$ Pa m, is higher than the force responsible for the lateral migration of magma. As a consequence, the lateral outward flow of magma is inhibited and the magma migrates inward toward the transfer zone, facilitating the development of the CD. Hence, although the ΔP_5 components are very similar, this process results in a marked asymmetry in the magma flow trajectories, which are strongly influenced by the initial asymmetric geometry of the magma chamber (Figure 5b).

[66] **Acknowledgments.** We thank two anonymous journal reviewers and the Associate Editor K. Stuewe for the careful and constructive revisions. We also thank J. M. Bartley, K. Benn, and C. Ebinger for the comments on an earlier version of the manuscript. We also express our gratitude to M. H. Dickson for improving the English text. G. Corti acknowledges financial support from CNR-Progetto Giovani Ricercatori-Agenzia 2000. D. Sokoutis thanks ISES (the Netherlands Center for Integrated Solid Earth Science) and NWO (the Netherlands Organization for Scientific Research) for the financial support.

References

Acocella, V., C. Faccenna, R. Funiciello, and F. Rossetti (1999a), Sand-box modelling of basement-controlled transfer zones in extensional domains, *Terra Nova*, *11*, 149–156.

Acocella, V., F. Salvini, R. Funiciello, and C. Faccenna (1999b), The role of transfer structures on volcanic activity at Campi Flegrei (southern Italy), *J. Volcanol. Geotherm. Res.*, *91*, 123–139.

Artyushkov, E. V. (1973), Stresses in the lithosphere caused by crustal thickness inhomogeneities, *J. Geophys. Res.*, *78*, 7675–7708.

Baker, B. H., P. A. Mohr, and L. A. J. Williams (1972), Geology of the Eastern Rift System of Africa, *Spec. Pap. Geol. Soc. Am.*, *136*, 67 pp.

Benes, V., and P. Davy (1996), Modes of continental lithospheric extension: Experimental verification of strain localization processes, *Tectonophysics*, *254*, 69–87.

Bonini, M., T. Souriot, M. Boccaletti, and J. P. Brun (1997), Successive orthogonal and oblique extension episodes in a rift zone: Laboratory experiments with application to the Ethiopian Rift, *Tectonics*, *16*, 347–362.

Bonini, M., D. Sokoutis, G. Mulugeta, M. Boccaletti, G. Corti, F. Innocenti, P. Manetti, and F. Mazzarini (2001), Dynamics of magma emplacement in centrifuge models of continental extension with implications for flank volcanism, *Tectonics*, *20*, 1053–1065.

Brune, J. N., and M. A. Ellis (1997), Structural features in a brittle-ductile wax model of continental extension, *Nature*, *387*, 67–70.

Buck, W. R. (1991), Modes of continental lithospheric extension, *J. Geophys. Res.*, *96*, 20,161–20,178.

Burov, E., and S. Cloetingh (1997), Erosion and rift dynamics: New thermomechanical aspects of post-rift evolution of extensional basins, *Earth Planet. Sci. Lett.*, *150*, 7–26.

Chu, D., and R. G. Gordon (1999), Evidence for motion between Nubia and Somalia along the Southwest Indian Ridge, *Nature*, *398*, 64–67.

Corti, G., M. Bonini, F. Innocenti, P. Manetti, and G. Mulugeta (2001), Centrifuge models simulating magma emplacement during oblique rifting, *J. Geodyn.*, *31*, 557–576.

Corti, G., M. Bonini, F. Mazzarini, M. Boccaletti, F. Innocenti, P. Manetti, G. Mulugeta, and D. Sokoutis (2002), Magma-induced strain localization in centrifuge models of transfer zones, *Tectonophysics*, *348*, 205–218.

Corti, G., M. Bonini, S. Conticelli, F. Innocenti, P. Manetti, and D. Sokoutis (2003), Analogue modelling of continental extension: A review focused on the relations between the patterns of deformation and the presence of magma, *Earth Sci. Rev.*, *63*(3–4), 169–247.

Cruden, A. R., H. Koyi, and H. Schmeling (1995), Diapiric basal entrainment of mafic into felsic magma, *Earth Planet. Sci. Lett.*, *131*, 321–340.

Daly, M. C., J. Chorowicz, and J. D. Fairhead (1989), Rift basin evolution in Africa: The influence of reactivated steep basement shear zones, in *Inversion Tectonics*, edited by M. A. Cooper and G. D. Williams, *Geol. Soc. Spec. Publ.*, *44*, 309–334.

Davis, M., and N. Kusznir (2002), Are buoyancy forces important during the formation of rifted margins?, *Geophys. J. Int.*, *149*, 524–533.

Davy, P., and P. R. Cobbold (1991), Experiments on shortening of 4-layer model of the continental lithosphere, *Tectonophysics*, *188*, 1–25.

Dewey, J. F. (1986), Diversity in the lower continental crust, in *The Nature of the Lower Continental Crust*, edited by J. B. Dawson et al., *Geol. Soc. Spec. Publ.*, *24*, 71–78.

Dunbar, J. A., and D. S. Sawyer (1989), Continental rifting at pre-existing lithospheric weaknesses, *Nature*, *242*, 565–571.

Ebinger, C. J. (1989a), Tectonic development of the western branch of the East African Rift System, *Geol. Soc. Am. Bull.*, *101*, 885–903.

Ebinger, C. J. (1989b), Geometric and kinematic development of border faults and accommodation zones, Kivu-Rusizi rift, Africa, *Tectonics*, *8*, 117–133.

Ebinger, C. J., and N. H. Sleep (1998), Cenozoic magmatism throughout east Africa resulting from impact of a single plume, *Nature*, *395*, 788–791.

Ebinger, C. J., A. L. Deino, R. E. Drake, and A. L. Tesha (1989), Chronology of volcanism and rift basin propagation: Rungwe Volcanic Province, East Africa, *J. Geophys. Res.*, *94*, 15,785–15,803.

Ellis, M., and G. King (1991), Structural control of flank volcanism in continental rifts, *Science*, *254*, 839–842.

England, P. C. (1983), Constraints on extension of continental lithosphere, *J. Geophys. Res.*, *88*, 1145–1152.

Fadaie, K., and G. Ranalli (1990), Rheology of the lithosphere in the East African Rift System, *Geophys. J. Int.*, *102*, 445–453.

Faulds, J. E., and R. J. Varga (1998), The role of accommodation zones and transfer zones in the regional segmentation of extended terranes, in *Accommodation Zones and Transfer Zones: The Regional Segmentation of the Basin and Range Provinces*, edited by J. E. Faulds and J. H. Stewart, *Spec. Pap. Geol. Soc. Am.*, *323*, 1–45.

Fleitout, L., and C. Froidevaux (1982), Tectonic and topography for a lithosphere containing density heterogeneities, *Tectonics*, *1*, 21–56.

Hill, R. I. (1991), Starting plumes and continental break-up, *Earth Planet. Sci. Lett.*, *104*, 398–416.

Huismans, R. S., Y. Y. Podladchikov, and S. Cloetingh (2001), Transition from passive to active rifting: Relative importance of asthenospheric doming and passive extension of the lithosphere, *J. Geophys. Res.*, *106*, 1271–1291.

Jackson, M. P. A., and B. Vendeville (1994), Regional extension as a geologic trigger for diapirism, *Geol. Soc. Am. Bull.*, *106*, 57–73.

Jones, C. H., J. R. Unruh, and L. J. Sonder (1996), The role of gravitational potential energy in active deformation in the southwestern United States, *Nature*, *381*, 37–41.

Kazmin, V., M. B. Seife, M. Nicoletti, and C. Petrucciani (1980), Evolution of the northern part of the Ethiopian Rift, in *Geodynamic Evolution of the Afro-Arabian Rift System*, *Atti dei Convegni Lincei*, vol. 47, pp. 275–292, Accad. Naz. dei Lincei, Rome.

Knott, S. D. (2001), Gravity-driven crustal shortening in failed rifts, J. Geol. Soc. London, 158, 193–196.

Lynch, H. D., and P. Morgan (1987), The tensile strength of the lithosphere and the localisation of extension, in *Continental Extensional Tectonics*, edited by M. P. Coward, J. F. Dewey, and P. L. Hancock, *Geol. Soc. Spec. Publ.*, *28*, 53–65.

Mahatsente, R., G. Jentzsch, and T. Jahr (1999), Crustal structure of the Main Ethiopian Rift from gravity data: 3-dimensional modeling, *Tectonophysics*, *313*, 363–382.

Mohr, P. A., and E. C. Potter (1976), The Sagatu Ridge dike swarms, Ethiopian rift margin, *J. Volcanol. Geotherm. Res.*, *1*, 55–71.

Morgan, P., W. R. Seager, and M. P. Golombek (1986), Cenozoic mechanical and tectonic evolution of the Rio Grande Rift, *J. Geophys. Res.*, *91*, 6263–6276.

Mulugeta, G. (1988), Squeeze-box in the centrifuge, *Tectonophysics*, *148*, 323–335.

Mulugeta, G., and W. Ghebreab (2001), Modeling heterogeneous stretching during episodic or steady rifting of the continental lithosphere, *Geology*, *29*, 895–898.

Petford, N., A. R. Cruden, K. J. W. McCaffrey, and J.-L. Vigneresse (2000), Granite magma formation, transport and emplacement in the Earth's crust, *Nature*, *408*, 669–673.

Ramberg, H. (1971), Dynamic models simulating rift valleys and continental drift, *Lithos*, *4*, 259–276.

Ramberg, H. (1980), Diapirism and gravity collapse in the Scandinavian Caledonides, *J. Geol. Soc. London*, *137*, 261–270.

Ramberg, H. (1981), *Gravity, Deformation and the Earth's Crust*, 452 pp., Academic, San Diego, Calif.

Ramberg, I. B., and P. Morgan (1984), Physical characteristics and evolutionary trends of continental rifts, *Proc. Int. Geol. Congr. 27th*, 165–216.

Ranalli, G. (1995), *Rheology of the Earth*, 2nd ed., 413 pp., Chapman and Hall, New York.

Rosendahl, B. L. (1987), Architecture of continental rifts with special reference to east Africa, *Ann. Rev. Earth Planet. Sci.*, *15*, 445–503.

Ruppel, C. (1995), Extensional processes in continental lithosphere, *J. Geophys. Res.*, *100*, 24,187–24,215.

Scholz, C. H., and J. C. Contreras (1998), Mechanics of continental rift architecture, *Geology*, *26*, 967–970.

Stüwe, K., and T. D. Barr (2000), On the relationship between surface uplift and gravitational extension, *Tectonics*, *19*, 1056–1064.

Ter Voorde, M., R. T. van Balen, G. Bertotti, and S. A. P. L. Cloetingh (1998), The influence of a stratified rheology on the flexural response of the lithosphere to (un),loading by extensional faulting, *Geophys. J. Int.*, *134*, 721–735.

Tommasi, A., and A. Vauchez (2001), Continental rifting parallel to ancient collisional belts: An effect of the mechanical anisotropy of the lithospheric mantle, *Earth Planet. Sci. Lett.*, *185*, 199–210.

Townsend, D. A., and L. J. Sonder (2001), Rheologic control of buoyancy-driven extension of the Rio Grande rift, *J. Geophys. Res.*, *106*, 16,515–16,523.

Versfelt, J., and B. R. Rosendahl (1989), Relationships between pre-rift structure and rift architecture in Lakes Tanganyika and Malawi, East Africa, *Nature*, *337*, 354–357.

Weijermars, R., and H. Schmeling (1986), Scaling of Newtonian and non-Newtonian fluid dynamics without inertia for quantitative modelling of rock flow due to gravity (including the concept of rheological similarity), *Phys. Earth Planet. Inter.*, *43*, 316–330.

WoldeGabriel, G., R. C. Walter, W. K. Hart, S. A. Mertzman, and J. L. Aronson (1999), Temporal relations and geochemical features of felsic volcanism in the central sector of the Main Ethiopian Rift, *Acta Volcanol.*, *11*, 53–67.

Zeyen, H., A. Negredo, and M. Fernàndez (1996), Extension with lateral material accommodation-'active' vs. 'passive' rifting, *Tectonophysics*, *266*, 121–137.

Ziegler, P. A., and S. Cloetingh (2003), Dynamic processes controlling evolution of rifted basins, *Earth Sci. Rev.*, *64*, 1–50.

M. Bonini, CNR–Istituto di Geoscienze e Georisorse, Sezione di Firenze, via G. La Pira, 4, I-50121, Florence, Italy.

S. Cloetingh and D. Sokoutis, Netherlands Center for Integrated Solid Earth Science, Faculty of Earth and Life Sciences, Vrije Universiteit Amsterdam, De Boelelaan 1085, NL-1081 HV, Amsterdam, Netherlands.

G. Corti and F. Innocenti, Dipartimento di Scienze della Terra, Università degli Studi di Pisa, via S. Maria 53, I-56126 Pisa, Italy. (cortigi@geo.unifi.it)

P. Manetti, CNR–Istituto di Geoscienze e Georisorse, via G. Moruzzi 1, I-56124 Pisa, Italy.

G. Mulugeta, Hans Ramberg Tectonic Laboratory, Institute of Earth Sciences, Uppsala University, Villavägen 16, SE-752 36 Uppsala, Sweden.